

1 **Terrain Trapped Airflows and Precipitation Variability during an**  
2 **Atmospheric River Event**

3

4 Ju-Mee Ryoo<sup>1,2,3</sup>, Sen Chiao<sup>3</sup>, J. Ryan Spackman<sup>1</sup>, Laura T. Iraci<sup>1</sup>, F. Martin Ralph<sup>4</sup>, Andrew  
5 Martin<sup>4</sup>, Randall M. Dole<sup>5,6</sup>, Josette E. Marrero<sup>1,7,8</sup>, Emma L. Yates<sup>1,7</sup>, T. Paul Bui<sup>1</sup>, Jonathan M.  
6 Dean-Day<sup>1,7</sup>, Cecilia S. Chang<sup>1,7</sup>

7 1 Earth Science Division, NASA Ames Research Center, Moffett Field, CA, USA

8 2 Science and Technology Corporation (STC), Moffett Field, CA, USA

9 3 San José State University, CA, USA

10 4 Center for Western Weather and Water Extremes, Scripps Institution of Oceanography, San  
11 Diego, CA, USA

12 5 CIRES, University of Colorado, Boulder, CO, USA

13 6 Earth System Research Laboratory, NOAA, Boulder, CO, USA

14 7 Bay Area Environmental Research Institute, Moffett Field, CA, USA

15 8 now at: Sonoma Technology, Petaluma, CA, USA

16

17

18 Revised to *Journal of Hydrometeorology*

19 **Corresponding author address:**

20 Ju-Mee Ryoo, Atmospheric Science Branch, NASA Ames Research Center, Moffett Field, CA

21 94035. Email: ju-mee.ryoo@nasa.gov

22

23 **Abstract**

24 We examine thermodynamic and kinematic structures of terrain trapped airflows (TTAs)  
25 during an Atmospheric River (AR) event impacting Northern California 10–11 March 2016  
26 using Alpha Jet Atmospheric eXperiment (AJAX) aircraft data, *in situ* observations, and Weather  
27 and Research Forecasting (WRF) model simulations. TTAs are identified by locally intensified  
28 low-level winds flowing parallel to the coastal ranges and having maxima over the near-coastal  
29 waters. Multiple mechanisms can produce TTAs, including terrain blocking and gap flows. The  
30 changes in winds can significantly alter the distribution, timing, and intensity of precipitation.  
31 We show here how different mechanisms producing TTAs evolve during this event and  
32 influence local precipitation variations.

33 Three different periods are identified from the time-varying wind fields. During Period 1  
34 (P1), a TTA develops during synoptic-scale onshore flow that backs to southerly flow near the  
35 coast. This TTA occurs when the Froude number ( $Fr$ ) is less than 1, suggesting low-level terrain  
36 blocking is the primary mechanism. During Period 2 (P2), a Petaluma offshore gap flow  
37 develops, with flows turning parallel to the coast offshore and with  $Fr > 1$ . Periods P1 and P2  
38 are associated with slightly more coastal than mountain precipitation. In Period 3 (P3), the gap  
39 flow initiated during P2 merges with a pre-cold frontal low-level jet (LLJ) and enhanced  
40 precipitation shifts to higher mountain regions. Dynamical mixing also becomes more important  
41 as the TTA becomes confluent with the approaching LLJ. The different mechanisms producing  
42 TTAs and their effects on precipitation pose challenges to observational and modeling systems  
43 needed to improve forecasts and early warnings of AR events.

44

## 45 **1. Introduction**

46 Extreme precipitation events have become more frequent and intense in recent years in  
47 California (Jain et al. 2005; Dettinger 2011). These events can cause hazardous and costly  
48 flooding impacts, but also contribute substantially to essential local water resources. Deleterious  
49 impacts were recently exemplified in California over the period of November 2016 – March  
50 2017, when numerous extreme precipitation events resulted in severe flooding. Along the U.S.  
51 West Coast, such extreme events often occur in conjunction with landfalling Atmospheric Rivers  
52 (ARs), which are characterized by elongated, deep, and narrow corridors of concentrated water  
53 vapor transport that form in the warm sector of extratropical cyclones (Zhu and Newell 1994,  
54 1998; Ralph et al. 2004, 2005a, 2006; Neiman et al. 2008; Dettinger et al. 2011a, b; Guan et al.  
55 2013; Ryoo et al. 2015). As ARs impinge upon the mountainous terrain along the west coast,  
56 heavy precipitation can be generated by orographic lifting of moist air on the windward slopes of  
57 the mountains and intensified further by convergence and vertical motions resulting from sub-  
58 synoptic interactions with terrain trapped airflows (TTAs) flowing parallel to the coastal ranges.

59 Terrain blocking is one mechanism for forming a TTA, with high static stability conducive  
60 to onshore flow turning parallel to rather than over higher terrain. The local blocking decelerates  
61 the flow, with pressure rises along the windward slopes. To balance the pressure gradient force  
62 normal to the barrier and the Coriolis force, the local disruption of the force balance (i.e.,  
63 geostrophic wind) leads to ageostrophic acceleration parallel to the barrier, resulting in a barrier  
64 jet (BJ), (Loescher et al. 2006). Pierrehumbert and Wyman (1995) found that the low-level  
65 terrain blocked flow often contains a BJ oriented parallel to the long axis of the high mountain  
66 range, which is maintained by a statically stable pressure ridge on the windward slope. Through  
67 modeling and a Froude number ( $Fr$ ) analysis, where  $Fr=U/Nh$  with  $U$  the barrier-normal wind

68 speed,  $h$  the barrier height, and  $N$  the Brunt-Väisälä frequency, Kim et al. (2007) showed the  
69 low-level water vapor transport by a BJ in a low- $Fr$  regime ( $Fr < 1$ ) accelerates northward  
70 moisture transport, resulting in a strong meridional precipitation gradient over the Sierra Nevada.  
71 More recently, Neiman et al. (2013) found that the Sierra Barrier Jets (SBJs) reach their  
72 maximum intensity during the strongest AR flow aloft, and that inland penetration of the AR  
73 through the San Francisco Bay gap in the coastal mountains maintains moist air transport by the  
74 SBJ. BJs due to low-level blocking are commonly observed with mountain ranges, including the  
75 Rocky Mountains (Colle and Mass 1995), the Sierra Nevada (Parish 1982; Neiman et al. 2010,  
76 2013, 2014), the coastal mountains of California (Doyle and Warner 1993; Doyle 1997; Yu and  
77 Smull 2000), the Appalachians (Bell and Bosart 1988), the European Alps (Chen and Smith  
78 1987), and the Alaskan coast (Olson et al. 2007).

79 TTAs can also form through mechanisms other than terrain blocking, such as with gap  
80 flows (Loescher et al. 2006; Valenzuela and Kingsmill 2015). Gap flows may develop when  
81 significant pressure and temperature differences are present between the entrance and exit of a  
82 low-elevation gap in a mountain range, leading to a local force imbalance and ageostrophic flow  
83 through the gap that often extends well beyond the gap exit. Using a mesoscale model,  
84 Steenburgh et al. (1998) examined a gap flow through a low-elevation gap in the Sierra Madre  
85 over the Gulf of Tehuantepec during a central American cold surge event (e.g., 12-14 March  
86 1993). The flow reached its maximum speed at the surface of  $\sim 25 \text{ m s}^{-1}$  offshore. Upon exiting  
87 the gap, the locally unbalanced flow turns anticyclonically due to the Coriolis force, becoming  
88 parallel to the terrain axis (Valenzuela and Kingsmill 2017).

89 TTAs associated with gap flows and their relationship to orographic precipitation over  
90 California have been examined in previous observational studies (Neiman et al. 2006;

91 Valenzuela and Kingsmill 2015, 2017). Neiman et al. (2006) identified relationships between  
92 Petaluma gap flow and rainfall over Bodega Bay in California using 915 MHz wind profiler  
93 observations during winter storms from 1997 to 2004. They found that rain rates and total  
94 rainfall increased over Bodega Bay in strong gap flow cases, and suggested that further  
95 understanding of relationships between the terrain-modulated flows and precipitation was needed  
96 to help improve forecasts. Using Doppler radar, Valenzuela and Kingsmill (2015) found that  
97 TTAs forced by the Petaluma gap flow enhanced precipitation over the ocean and near the coast.  
98 They demonstrated how TTAs could combine with pre-cold frontal low-level jets (LLJs). These  
99 pre-cold frontal LLJs are sub-synoptic scale features occurring within many extratropical  
100 cyclones, and are characterized by relatively warm temperatures, weak stratification, high water  
101 vapor content, and strong low-altitude winds (Browning and Pardoe 1973; Ralph et al. 2005a). In  
102 the Valenzuela and Kingsmill (2015) study, profile sounding data, while of great value, was  
103 limited to observations at single points. Thus, these observations could not determine whether  
104 mixing was occurring at the pre-cold frontal LLJs and TTA interface or interactions with the  
105 synoptic LLJ and topography. Such questions motivated us to augment the new observations  
106 reported in this study with dynamical diagnostic analyses and regional model simulations.

107 Prior modeling studies have helped greatly to clarify the fundamental connections between  
108 sub-synoptic low-level jets, orographically-modified flows, and precipitation, as well as to reveal  
109 gaps in our current understanding, observations and modeling capabilities. Doyle (1997) showed  
110 for a storm system impacting the northern California coast in January 1995 that the mesoscale  
111 precipitation structure was simulated reasonably well, but with a slight discrepancy between the  
112 observed and the simulated orientation of the frontal rainband. Using the high-resolution fifth-  
113 generation Pennsylvania State University–National Center for Atmospheric Research (NCAR)

114 Mesoscale Model (MM5) (MM5, Grell et al. 1995), Olson et al. (2007) also showed that the  
115 model simulation adequately reproduced the southeastern Alaskan coastal jets, low-level  
116 pressure perturbations, and orographic flow response, but had a timing bias associated with the  
117 approach of a pressure trough, and a magnitude bias for precipitation. Ongoing questions related  
118 to understanding and modeling precipitation timing, magnitude, and location are vital to  
119 improving early warnings and forecasting impacts, helping to motivate the research reported here.

120 Here, we first examine mechanisms for the formation of TTAs and associated changes in  
121 wind fields over Northern California during an AR event occurring over the period of 10-11  
122 March 2016. Both observational and modeling approaches are employed, including aircraft  
123 observations, surface wind profiler observations, reanalysis data, and a high-resolution (1-km)  
124 Advanced Research Weather Research and Forecasting model (ARW-WRF) simulation.  
125 Temporal and spatial variations in winds and precipitation are also examined, and they are  
126 related to the different mechanisms for TTA formation and large-scale mixing during the AR  
127 event. Our central hypothesis is that wind speed and direction are closely related to different  
128 processes of TTA formation and that these differences have discernible impacts on the location  
129 and intensity of precipitation during an AR event. We evaluate this hypothesis by comparing  
130 observations with model simulations and performing diagnostic analyses of stability, force  
131 balance, and dynamical mixing relationships during the evolution of this AR event.

132 The following section provides details on the experimental design, observational and model  
133 data, and methods used in this study for an AR case that impacted the northern and central  
134 California coast on 10-11 March 2016. Subsequent sections then describe observations of TTAs ,  
135 their relationships to time-varying synoptic and precipitation features, and comparisons with  
136 model results. The last section summarizes primary findings and implications from this study.

137

## 138 **2. Experimental Design**

### 139 *a. Airborne instrumentation and flight plan*

140 To map out the structure and gradients of water vapor and wind in the mid- and low-  
141 troposphere in the coastal region south of San Francisco Bay, *in-situ* measurements of water  
142 vapor and 3-D winds were collected during a flight originating from Moffett Field, CA (37.42°N,  
143 122.05°W). The aircraft performed six consecutive level flight legs (see Figs. 1 and 3) between  
144 14:50 and 16:05 Pacific Standard Time (PST) on 10 March 2016 (22:50 UTC through 00:05  
145 UTC; AJAX flight #181). Offshore level legs were executed at multiple altitudes (0.03, 0.2, 1.2,  
146 2.4, and 3.1 km), paralleling the coast from as far north as conditions allowed at each altitude  
147 and continuing in a straight line to the southeast, extending nearly to Pt. Sur, CA. The final leg  
148 was executed closer to shore, spanning the mouth of Monterey Bay and then paralleling the  
149 original flight line but closer to shore. Water vapor volume mixing ratio is measured with a  
150 commercial instrument employing cavity ringdown spectroscopy (CRDS) and data for the flight  
151 reported here. H<sub>2</sub>O is estimated to have an uncertainty of < 4-6%, depending on the amount of  
152 water vapor present (Filges et al. 2015). For this study, these values are converted into H<sub>2</sub>O mass  
153 (g kg<sup>-1</sup>) mixing ratios.

154 As part of the Alpha Jet Atmospheric eXperiment (AJAX), the Meteorological Measurement  
155 System (MMS; Scott et al. 1990; Gaines et al. 1992) provided high-resolution pressure,  
156 temperature, and 3-D (u, v, and w) wind measurements. This instrument consists of three major  
157 systems: (1) an air motion sensing system to measure the air velocity with respect to the aircraft,  
158 (2) an aircraft motion sensing system to measure the aircraft velocity with respect to the earth

159 surface, and (3) a data acquisition system to sample, process, and record the measured quantities.  
160 Further details of the complete airborne facility are presented in Hamill et al. (2016).

161

162 *b. Other instrumentation and datasets*

163 National Oceanic and Atmospheric Administration (NOAA) 449 MHz surface wind profiler  
164 data collected at the Bodega Bay, California (BBY, 38.3 °N, 123.1°W, elev. 15 m) site were used  
165 in this study. This radar wind profiler detects a Doppler shift due to air motion to obtain wind  
166 speeds and directions from 180 m above the ground surface up to 8 km, depending on  
167 atmospheric conditions. Together with this, the Global Positioning System Meteorology (GPS-  
168 Met), a ground-based water vapor observing system measuring atmospheric total-column  
169 integrated precipitable water vapor, is collocated with the existing Hydrometeorology Testbed  
170 (Ralph et al. 2005b; HMT-West) wind profiler at the BBY site (White et al. 2013). At BBY  
171 (coastal), additional hourly observations of integrated water vapor, total wind speed, wind  
172 direction, total integrated water vapor flux, upslope wind speed and direction, and upslope  
173 integrated water vapor (IWV) flux were provided by the NOAA Physical Science Division  
174 (PSD) (<https://www.esrl.noaa.gov/psd/data/obs/datadisplay/>). Coastal precipitation (at BBY) and  
175 mountain precipitation (at Cazadero, California (CZD), 38.6 °N, 123.2 °W, elev. 478 m) data  
176 from tipping bucket measurement (White et al. 2013) were also provided by NOAA PSD. Since  
177 IWV fluxes are closely linked to orographic precipitation (Neiman et al. 2002), we used the  
178 upslope IWV fluxes to show the strength of the water vapor fluxes orthogonal to the axis of the  
179 coastal mountains and examine relationships to temporal precipitation variability over coastal  
180 and mountainous regions during the course of the AR event.



181 MERRA-2 reanalyses were used for constructing synoptic-scale analysis and diagnostic  
182 fields during the AR event. MERRA-2 is a NASA atmospheric reanalysis for the satellite era  
183 using the Goddard Earth Observing System Model, Version 5 (GEOS-5) with its Atmospheric  
184 Data Assimilation System (ADAS), version 5.12.4. The MERRA-2 horizontal winds ( $u$ ,  $v$ ),  
185 vertical wind ( $\omega$ ), and temperatures are reported at a horizontal resolution of  $0.66^\circ$  longitude  
186 by  $0.5^\circ$  latitude on 42 pressure levels spanning from 1000 to 0.01 hPa, at 3-hourly time  
187 resolution. See Bosilovich et al. (2016) for further details regarding the MERRA-2 reanalyses.

188

### 189 *c. Model simulations*

190 All model simulations here were conducted with the Advanced Research Weather Research  
191 and Forecasting (WRF-ARW) model version 3.8. (Skamarock et al. 2008). Prior studies have  
192 used the WRF-ARW to investigate Atmospheric River events over Northern California (Eiserloh  
193 and Chiao 2015; Martin et al. 2018). Eiserloh and Chiao (2015) showed that this model was able  
194 to reproduce well monthly precipitation and snowfall over this region. Initial and time-dependent  
195 lateral boundary conditions were supplied from NCEP North American Mesoscale Forecast  
196 System (NAM) analyses at 12 km horizontal resolution. The simulation was initialized at 1200  
197 UTC 9 March 2016 and run for 72 h until the end of the AR event at 1200 UTC 12 March. The  
198 selected horizontal grid spacing was 1 km, with 41 vertical levels. The Thompson graupel (2-  
199 moment) microphysics scheme (Thompson et al. 2004) and the Yonsei University (YSU)  
200 boundary layer microphysics scheme (Hong et al. 2006) were used. The Thompson scheme was  
201 chosen because it has been shown to produce a smaller wet-bias in cold season Quantitative  
202 Precipitation Forecasting (QPF) over portions of northern California than other popular  
203 microphysics schemes in WRF (Jankov et al. 2007). The Noah land surface model (Ek et al.

204 2003), the Goddard scheme for shortwave radiation (Chou and Suarez 1994), and the Rapid  
205 Radiative Transfer Model (RRTM) scheme for longwave radiation (Mlawer et al. 1997) were  
206 also employed.

207 A Q diagnostic was used as a measure of the relative contribution of strain and rotation in  
208 the large-scale flow to identify whether the horizontal dynamical mixing may be significant.  
209 Here,

$$210 \quad Q = \frac{1}{2} \left( \frac{1}{\cos\varphi} \frac{\partial u}{\partial \lambda} - v \tan\varphi \right)^2 + \frac{1}{2} \left( \frac{\partial v}{\partial \varphi} \right)^2 + \frac{\partial u}{\partial \varphi} \left( \frac{1}{\cos\varphi} \frac{\partial v}{\partial \lambda} + u \tan\varphi \right)$$

211 where  $\lambda$  and  $\varphi$  are longitude and latitude, respectively (Haynes 1990; Fairlie et al. 2007). This  
212 measure has been used in studies of intermediate to small-scale variability in the troposphere to  
213 examine dynamical mixing, such as during upper-level Rossby wave breaking in the upper-  
214 troposphere. Here large positive Q values suggest increased strain with enhanced mixing, while  
215 small and negative Q values indicate dominance of rotation of the flow with reduced mixing.

216

#### 217 *d. Locations of measurements, flight track, and AR event*

218 Figure 1a shows a map of the study region and the AJAX flight track for the AR event on  
219 10 March 2016. The map also identifies the wind profiler site (BBY), the mountain precipitation  
220 site (CZD), and the Petaluma gap. The inset plot shows the spatial variability of water vapor in  
221 the offshore region measured from the aircraft. Aircraft data were collected from the surface to  
222 ~3.1 km (~10 kft). Level leg flight data show that water vapor is higher at low altitudes than at  
223 higher altitudes. A similar flight to the north of San Francisco Bay was performed on 9  
224 December 2015, but the lower level legs were limited by flight constraints of reduced visibility  
225 and air traffic control restrictions, with no TTAs features found (not shown).

226 Bands of low brightness temperature in satellite imagery (Fig. 1b), suggestive of deep  
227 convective clouds and surface rainfall show the signature of an AR event (Galewsky and Sobel  
228 2005) extending from the eastern Pacific to the western U.S. Based on the Integrated Water  
229 Vapor (IWV) and Integrated Water Vapor Flux (IVT) computed from MERRA-2, this event  
230 meets the three quantitative detection criteria for defining an AR: 1)  $IVT > 500 \text{ kg m}^{-1} \text{ s}^{-1}$ , 2)  
231 width  $< 1000 \text{ km}$ , and 3) length  $> 1500 \text{ km}$ , where IVT is computed as  $IVT = \frac{1}{g} \int_0^p q \cdot \vec{U} dp$ , with  $g$   
232 the acceleration of gravity,  $q$  the specific humidity,  $\vec{U} = (u, v)$  the horizontal wind, and  $p$  the  
233 pressure, with integration performed over the pressure levels from 1000 hPa to 300 hPa. Similar  
234 evaluations performed with the NCEP reanalysis (Rutz et al. 2014) and Global Forecast System  
235 (GFS) model (Wick et al. 2013a, b) were consistent in identifying this event as satisfying the AR  
236 criteria.

237

### 238 **3. Synoptic conditions and the observed characteristics of the TTA**

239 Lower-tropospheric wind maxima that are often observed in the coastal zone can be  
240 enhanced by coastal orography due to BJs (Bell and Bosart 1988; Doyle and Warner 1993;  
241 Doyle 1997). TTAs can be forced by either onshore or offshore flow at the coast at various  
242 altitudes (Doyle 1997; Olson et al. 2007; Valenzuela and Kingsmill 2015). To examine how a  
243 specific synoptic condition can provide favorable conditions for generating a TTA and how the  
244 flow evolves during an AR event, we first provide a synoptic overview for this AR event.

245

#### 246 *a. Synoptic conditions*

247 Figure 2 shows the evolution of specific humidity ( $q$ ), horizontal wind, temperature (T) at

248 700 hPa; sea level pressure, and potential vorticity (PV) at 500 hPa for the AR period of 10-11  
249 March 2016 using MERRA-2 reanalysis data. As the AR approaches the western U.S., a robust  
250 upper-level trough associated with high PV ( $> 1$  potential vorticity units, PVU) at 500 hPa is  
251 located offshore near the coast of CA. In advance of this system, strong low-level southerlies and  
252 southwesterlies are present over the coast of CA with relatively dry airmass. The advancing deep  
253 trough is similar to the synoptic situation described by Colle et al. (2006), who found that cold  
254 season BJs are associated with an anomalously deep large-scale upper-level trough approaching  
255 the coast. Similar features are found at 850 hPa (not shown). By 2100 UTC 10 March, the high  
256 and narrow water vapor band is elongated from southwest to northeast with strong  
257 southwesterlies and relatively warmer temperature inland (Figs. 2(a, d)) compared to later in the  
258 event. At the surface, low pressure is centered over the eastern North Pacific, with southwesterly  
259 flow extending toward the CA coast (Fig. 2g). PV in the deep upper trough has values exceeding  
260 1.5 PVU, suggesting that of the dynamical tropopause extends downward to at least 500 hPa. On  
261 0900 UTC 11 March, the dominant flow is still southwesterly (Fig. 2b), but a southerly  
262 component has increased and the horizontal wind has become more meridionally oriented, as has  
263 the elongated band of high water vapor associated with the AR. The main axis of relatively cold  
264 air aloft has a small center situated well offshore the CA coast associated with the high PV air in  
265 the mid-troposphere (Figs. 2(e, h)). The region of maximum horizontal temperature gradient  
266 shifts farther south, and temperatures are slightly cooler inland north of the San Francisco Bay  
267 Area.

268 By 1800 UTC 11 March, higher water vapor has moved inland along with cooler  
269 temperatures, and the surface low and upper-level PV trough have weakened (Figs. 2i).  
270 Interestingly, the strong upper level trough shown on 10 March appears to undergo anticyclonic

271 Rossby wave breaking (Fig. 2g). Ryoo et al. (2015) demonstrated that 66% of the AR events  
272 from 1997-2010 were associated with anticyclonic Rossby wave breaking, and those AR events  
273 appear closely linked to this upper-level dynamical evolution. The large-scale upper-level  
274 troughs over northern California may also provide favorable conditions for the formation of  
275 TTAs during AR events.

276

277 *b. Observed vertical profiles of AJAX measurements*

278 Consistent with the MERRA-2 data shown in Fig. 2a, the predominant wind direction  
279 measured *in situ* was southwesterly at about 2300 UTC (Fig. 3b). However, there is a subtle  
280 shift in horizontal winds at the lowest level, particularly evident in the northern part of the  
281 transect (around 37-37.2°N, 122.4°W), with winds deflecting northward to more parallel to the  
282 coast (red circles in Figs. 3(b, c)). This turning of wind direction along the transect from the  
283 southeast (SE) to the northwest (NW) appears to be a signature of the emergence of the first TTA  
284 during this AR event, and is manifest also in the evolving water vapor flux. The time series of  
285 water vapor and winds measured by AJAX over all altitudes are shown in Fig. S1 in  
286 Supplemental Materials.

287 TTAs due to low-level blocking may occur during low  $Fr$  conditions,  $Fr < 1$ , with favorable  
288 synoptic conditions characterized by relatively weak large-scale cross-barrier flow and relatively  
289 high static stability (recall that  $Fr=U/Nh$  with  $U$  the barrier-normal wind speed,  $h$  the barrier  
290 height, and  $N$  the Brunt-Väisälä frequency). In the most straightforward analysis,  $Fr$  is estimated  
291 using the dry Brunt- Väisälä frequency,  $N_d^2 = g/\theta(d\theta/dz)$ , where  $\theta$  is potential temperature, and  $g$   
292 is an acceleration of gravity. Many studies, however, have shown that moist Brunt-Väisälä  
293 frequency ( $N_m$ ; Durran and Klemp 1982; Hughes et al.; 2009) is a more appropriate choice when

294 air impinging on mountains is saturated. Since  $N_m$  is only applicable in saturated conditions,  $N_m$   
295 is used here only when the near-surface ( $< 500$  m altitude) relative humidity (RH) exceeds 90%;  
296 otherwise,  $N_d$  is used.

297 Figure 3d shows in-situ wind speeds and  $Fr$  values. On March 10, the meridional wind is 5–  
298  $10 \text{ m s}^{-1}$  higher than the zonal wind, especially around about 1 km above ground level (agl) (not  
299 shown). Since the coastal mountains just inland approximately parallel the coastline, we estimate  
300 the terrain-parallel wind by the coast-parallel wind component. The horizontal wind components  
301 ( $\vec{U} = (u, v)$ ), the angle ( $\beta$ , about  $56.3^\circ$ ) between the coastline from the North direction, and the  
302 angle ( $\alpha$ , where  $\alpha = \tan^{-1}\left(\frac{v}{u}\right) - \beta$ ) between the horizontal wind vector and the line normal to  
303 the coastline are used for computing the terrain-parallel component and terrain-normal  
304 component of the wind near Mt. Santa Cruz. AJAX measures the potential temperatures ( $\theta$ ) with  
305 respect to altitude, longitude, latitude, and time. At the given location where there is vertical  
306 transect, we calculated the vertical potential temperature gradient by calculating ( $\partial\theta/\partial z$ ). The  
307 terrain-parallel wind increases at the lowest altitude and between 0.4–0.9 km agl (red profile in  
308 Fig. 3d). As mentioned earlier, we observed the initial development of the wind deflection to be  
309 parallel to the coast, identifying the formation of the initial CBJ (the first TTA) from AJAX data.  
310 The increasing terrain-parallel wind occurs during a period when  $Fr < 1$ , consistent with this CBJ  
311 being due primarily to low-level terrain blocking related to the relatively weak onshore flow and  
312 high static stability at lower levels during this period.

313 The topographic effect of terrain blocking on the wind field occurs within a Rossby radius of  
314 deformation of the topography,  $L$  (Gill 1982; Luna-Niño et al. 2017), where  $L = (N^*h)/f$ , with  $f$   
315 being the Coriolis parameter (Valenzuela and Kingsmill 2018). When low-level terrain blocking

316 exists (i.e.,  $Fr < 1$ ),  $L$  is an order of  $\sim 100$  km or less for a terrain height in the coastal region ( $\leq 1$   
317 km),  $N$  of  $0.01 \text{ s}^{-1}$ , and  $f$  about  $10^{-4} \text{ s}^{-1}$ ). For computing  $Fr$ , we used the observed terrain-normal  
318 wind as  $U$ . The transect AJAX flew was  $\leq 15$  km off the California coast (except when crossing  
319 the mouth of Monterey Bay), so the measured winds were generally affected by topography, and  
320 well within  $L$ . Although ideally, upstream cross-barrier observed winds should be used for  $U$  to  
321 compute  $Fr$ , the mean velocity of the upstream flow appeared to be slightly less than or the same  
322 as near the coast around 20-23 UTC 10 March, especially during the period when terrain  
323 blocking occurs (supported by the model simulation, not shown). Therefore, uncertainties in  
324 choice of the upstream winds for estimating  $Fr$  are unlikely to affect this interpretation.

325

326 *c. Observed TTAs from NOAA-wind profilers and precipitation measurements*

327 Augmenting observations of the first TTA from AJAX flight measurements, which suggest a  
328 terrain blocking mechanism, we further examined the characteristics of TTAs during this AR  
329 event using wind profilers and hourly rain rates at BBY during the period 10-11 March 2016 (Fig.  
330 4). Around 2300 UTC 10 March, the wind below 0.5 km starts changing its direction toward  
331 southeasterly, approximately parallel to the coastal terrain. The southeasterly signature persists  
332 between 2300 UTC on 10 March and roughly 1800 UTC on March 11, developing from lower  
333 altitudes of  $\sim 0.4$  km up to 1.4 km above the surface.

334 To better identify distinct mechanisms related to TTAs occurring during the AR, we divide  
335 the AR into three sub-periods based on wind fields, with key differences summarized in Table 1.  
336 Period 1 (P1) is identified when the low-level wind ( $< \sim 800$  m) is southeasterly with speed less  
337 than  $5 \text{ m s}^{-1}$ , occurring during 2100-2300 UTC 10 March 2016. During this period, there is also  
338 a deflected wind toward the coast in the 10-meter modeled wind field nearest the aircraft transect

339 (see Fig. 7a). Period 2 (P2, 0500-0900 UTC 11 March) is defined when the low-level wind ( $< \sim$   
340 800 m) is southeasterly with speed  $< 15 \text{ m s}^{-1}$ , and strong onshore (westerly and southwesterly)  
341 flow occurs above 1 km. Period 3 (P3) is defined when the low-level wind ( $< \sim 800 \text{ m}$ ) is still  
342 southeasterly but with wind speed  $> 15 \text{ m s}^{-1}$ , which captures the time between 1000 UTC -1800  
343 UTC 11 March 2016. The strongest low-level winds occur during P3 at  $\sim 1.2 \text{ km}$  above the  
344 surface at 1500–1600 UTC 11 March, related to the pre-cold frontal LLJ (see Fig. 4a).

345 All these wind features are associated with locations of enhanced precipitation during the  
346 different periods. Mountain precipitation (green bars in Fig. 4b) is abundant during 1000-2100  
347 UTC, but begins to diminish around the time when the weak southeasterlies emerge (2300 UTC  
348 10 March, P1) and does not return until 0900 UTC 11 March as P2 ends. The upslope IWV  
349 fluxes (blue line) weaken during the early period of southeasterlies (2300 UTC 10 March) but  
350 strengthen again around 0900 UTC and 1500 UTC 11 March. The upslope wind speeds and IWV  
351 fluxes closely correspond (not shown). During P1, the coastal precipitation increases (red bars),  
352 in contrast with the mountain precipitation. Coastal precipitation also increases during the end of  
353 P2. During P3, mountain precipitation increases as upslope IWV flux (and wind speed) increases.  
354 Finally, after 1800 UTC 11 March, the wind direction turns to southwesterly, and the upslope  
355 IWV flux significantly decreases, leading to an overall reduction of precipitation. The winds and  
356 IWV flux patterns in Fig. 4 are consistent with the observed precipitation features over the BBY  
357 (coastal area) and the CZD (mountain area) sites.

358

#### 359 *d. Model-observation comparison*

360 The upper panels in Fig. 5 show vertical profiles of zonal wind, meridional wind, and  
361 potential temperature measured by i) AJAX and the WRF model simulation interpolated along



362 the flight track for 2200-2400 UTC 10 March 2016, and ii) wind profiler and WRF model  
363 simulation interpolated along the wind profiler at 1100 UTC 11 March 2016. Most features of  
364 the model simulation are within the range of observed winds and potential temperatures. There  
365 are, nevertheless, some notable differences. The model tends to underestimate the observed  
366 meridional wind below 1.5 km while it overestimates the observed winds above 2 km.  
367 Discrepancies are found between the observations and WRF simulation in zonal wind shear  
368 between 500 m and 2 km (see Fig. 5a). Possible contributors to the differences are: 1)  
369 Inadequacies in simulating vertical shear related to the TTA from low-level terrain blocking.  
370 Notably, the wind profiler at 2300 UTC over BBY also indicated some disagreement with WRF  
371 winds below 2km (not shown). 2) Possible underestimation in the WRF model of the shear layers  
372 and shear-generated turbulence of the low-level blocked flow at these levels (Houze and Medina,  
373 2005), so that the model fails to adequately capture the presence of the CBJ around 800 m and  
374 above it (1.5 km) over Mt. Santa Cruz at the time of measurement. A similar discrepancy was  
375 found between the model and BBY wind profiler data comparison at the same time (~ 2300 UTC  
376 10 March 2016). 3) Model potential temperatures also tend to be warmer than observations  
377 except below 0.5 km, indicating low-level static stability is higher in the model than observations,  
378 which may contribute to simulation and prediction errors. Due to the different temporal and  
379 spatial resolution and data availability, a direct comparison between the WRF model and AJAX  
380 data is also challenging to make. While these model-observation discrepancies are notable and  
381 merit additional study, the overall ability of the model simulation to replicate most observed  
382 wind and potential temperature features supports our interpretation for many important processes  
383 during this event.

384 Figure 6 shows the comparison of average wind speed (up to 5 km from the surface) and 1-  
385 hourly rain rate, from both observation (red) and WRF model simulation (blue). The model wind  
386 overestimates observed values by 2-4 m s<sup>-1</sup> around 1900 UTC 10 March and 0100 UTC 11  
387 March, but otherwise, has similar features and magnitudes. In general, model precipitation over  
388 BBY overestimates observed precipitation, although the overall pattern can replicate the  
389 observed pattern for some periods. Model precipitation over CZD generally lags behind observed  
390 precipitation during P2 and P3, and it may underestimate precipitation totals. The ratio of  
391 mountain (CZD) to coastal (BBY) rain (bottom panel) has higher values (> 2.5 on average)  
392 starting from ~1000 UTC 11 March to the 1800 UTC 11 March, corresponding to P3. Slightly  
393 lower values (< 1.5 on average) over P1 and P2 are found. This is consistent with the results of  
394 Valenzuela and Kingsmill (2017), who reported coastal precipitation (i.e., at BBY) tends to  
395 increase when TTAs are developing. We also compared the maps of 6-hourly accumulated  
396 NCEP-Stage IV precipitation (Nelson et al., 2016;  
397 <http://www.emc.ncep.noaa.gov/mmb/ylin/pcpanl/stage4/>) and WRF simulated precipitation  
398 during the 10–11 March 2016 AR case in Fig. S2 in the Supplemental Materials. In general,  
399 NCEP-Stage IV and modeled precipitation show similar features regarding variability, except for  
400 the Sierra Nevada mountain region and the coastal range, where both measuring and predicting  
401 precipitation over mountainous regions pose particular challenges (Strangeways 1996; Smalley  
402 et al. 2013).

403

#### 404 **4. Characteristics of TTAs simulated from WRF-ARW**

405 *a. Kinematic characteristic of TTAs*

406 To further understand the detailed kinematic structure and characteristics of TTAs in  
407 conjunction with the pre-cold frontal LLJs, we examined time-series of modeled meridional  
408 wind and precipitation at both BBY, CZD, and Mt. Santa Cruz in Fig. 7. The closest distance  
409 from the AJAX flight track to Mt. Santa Cruz (peak elev.  $\sim 1154$  m) was  $\sim 40$  km, and a second  
410 peak (elev.  $\sim 740$  m) was also located  $\sim 15$  km from the flight track. Over Mt. Santa Cruz (Fig.  
411 7b), the modeled wind does not indicate southeasterly flow until around 0500 UTC 11 March, in  
412 comparison to the in-situ observation of southeasterly wind emerging around 2300 UTC 10  
413 March (see red circle in Fig. 4). This is consistent with the results shown in Fig. 5a, highlighting  
414 the difficulty in modeling low-level zonal wind shear between 500 m and 2 km in this event.

415 Figure 7a shows a distinctive vertical gradient of meridional wind speed at BBY at this time,  
416 centered  $\sim 1$  km aloft, with values of  $\sim 5$  m s<sup>-1</sup> below and 25 m s<sup>-1</sup> above. At BBY, different wind  
417 patterns (wind direction and wind speed) were observed over two periods: 2100  $\sim$  2300 UTC 10  
418 March (identified as P1), and 0500  $\sim$  0900 UTC 11 March (identified as P2). Consistent to Fig. 4,  
419 around 2300 UTC 10 March (during P1), the surface winds were mainly southeasterly, and a pre-  
420 cold frontal LLJ structure was absent. The zonal wind (easterly) patterns showed that the airflow  
421 was directed approximately parallel to the coastal mountains from SE to NW, consistent with a  
422 CBJ (Fig. 7a). Around 0500 UTC 11 March (during P2), a meridional pattern similar to that  
423 around 2300 UTC 10 March was also found with a strong jet structure and relatively dry air (low  
424 specific humidity,  $q$ , not shown). The potential temperature decreases with time toward the end  
425 of P3, indicating a cold front passage after the AR event (not shown). Both observational and  
426 model data show more coastal precipitation (BBY) than mountain precipitation (CZD and Mt.  
427 Santa Cruz) during P1 and P2 (Figs. 4, 6, and 7). Conversely, mountain precipitation is slightly  
428 more abundant during P3 (CZD) and after (Mt. Santa Cruz, Figs. 7(c, d)). This is consistent with

429 the finding of Valenzuela and Kingsmill (2017), who showed that the mountain-to-coast rainfall  
430 ratio was lower ( $\sim 1.4$ ) when there was terrain trapped flow (TTA), while the ratio increased  
431 ( $\sim 3.2$ ) without TTA.

432 To further understand the processes of TTA formation, we examined the WRF model flow  
433 patterns, temperatures, and wind speeds during two different periods. Figure 8 (a, b, c) shows the  
434 WRF-simulated surface temperature overlaid by 10-meter wind vectors; panels (d, e, f) show 10-  
435 meter wind speed (colors) and sea level pressure (isobars). On 2300 UTC 10 March (Figs. 8(a, d),  
436 corresponding to P1), relatively warm and mild onshore-directed southwesterly flow is evident  
437 that changes direction to parallel the coast, forming a weak CBJ (the first TTA). At this time, the  
438 precipitation over the coastal region north of San Francisco Bay increases slightly (Figs. 7(c, d),  
439 Fig. 8g). Consistent with the  $Fr$  analysis using aircraft data shown in Fig. 3,  $Fr$  values computed  
440 from model data are  $< 1$  at the north of San Francisco bay area including BBY and Mt. Santa  
441 Cruz around 500 m at 2300 UTC 10 March, supporting the earlier interpretation of terrain flow  
442 blocking for this TTA event.

443 From 0500 UTC 11 March to 0900 UTC 11 March (corresponding to P2), more organized  
444 southeasterly flow develops parallel to the coastline (Fig. 8b). Offshore-directed gap flow from  
445 the Central Valley turns anticyclonically near the coast, further contributing to a strong TTA (the  
446 second TTA). Relatively cold air exited from the interior through the Petaluma gap and crossed  
447 over BBY, augmenting the gap flow due to pressure gradients associated with approaching  
448 synoptic-scale AR storm (Figs. 8(b, e)). Note that the maximum speed of the offshore-directed  
449 gap flow tends to be 2-3 times larger than that of the ambient synoptic flow (see Fig. 8b). This  
450 implies that the gap flow can determine the size of TTA, consistent with Olson et al. (2007),  
451 which a gap flow can extend the size of BJ by changing its structure and intensity over the

452 southeast Alaskan coast. Precipitation increases over the area where the temperature gradient is  
453 large and tends to increase over the coastal region (Fig. 8h).

454 On 1700 UTC 11 March (Figs. 8(c, f), corresponding to P3), confluence of the synoptic  
455 flow offshore with gap winds is located near the coast, especially south of Mt. Santa Cruz and  
456 Monterey Bay, leading to strong wind speeds combined with high water vapor transport (not  
457 shown). This combination can lead to high precipitation rates over favored mountain regions, as  
458 shown in Fig. 8i. Over the three periods throughout this AR event, different wind directions and  
459 speeds associated with the TTAs were closely related to precipitation patterns and intensities  
460 over the coastal and mountain regions.

461

462 *b. Forcing mechanisms of TTAs: low-level blocking and gap flow*

463 To confirm that the TTA occurring during P2 is produced by the Petaluma gap flow, we  
464 examined the relationship between the pressure gradient and wind at BBY to determine if this  
465 event followed the theoretical relationship shown by Valenzuela and Kingsmill (2015, 2018).  
466 The hourly pressure difference was calculated between BBY and Stockton, located at the eastern  
467 end of the Petaluma gap. Zonal winds were derived using the simulated 0-500 m layer-mean  
468 winds and 10-meter wind. Figure 9a shows the hourly model data, with different symbols  
469 representing P1, P2, P3, and post-P3 periods. The solid line shows the theoretical relationship  
470 used to derive the gap flow as a function of the pressure gradient (Mass et al. 1995). We include  
471 the frictional effects using the same drag coefficient used in Mass et al. (1995). The boundary  
472 layer depth (PBLH) is estimated as 700 m, and the average air density of  $1.24 \text{ kg m}^{-3}$  was chosen  
473 based on the observations at BBY and Stockton, used in Valenzuela and Kingsmill (2017).  
474 Sensitivity of the result to different PBLH (500m, 700m, and 1000m) was small (not shown).

475 We focus first on the period from 0500 - 1800 UTC 11 March during P2, when the second  
476 TTA forms, and P3, when the TTA merges with the pre-cold frontal LLJ. Figure 9a shows that  
477 the model data agrees with the theoretical force balance relationship between the pressure  
478 difference and the zonal wind due to gap flow. In contrast, the conditions before 0500 UTC (P1,  
479 open squares) and after 1900 UTC 11 March (post-P3, filled triangles) significantly depart from  
480 the relationship, indicating that these periods are not associated with gap flow.

481 Figure 9b shows  $Fr$  calculated using WRF-simulated wind during different analysis periods  
482 and its sensitivity to the terrain height. The upstream wind ( $U$ ) is less than  $\sim 8 \text{ m s}^{-1}$ , and  $N$  is  $\sim$   
483  $0.01 \text{ s}^{-1}$  over the area averaging both BBY and CZD during P1 (open squares). The  $Fr$  shows that  
484 the flow has low  $U/Nh$  (i.e.,  $Fr < 1$ ) when the mountain height ( $h$ ) is set to 0.5, 0.8, or 1 km.  
485 This indicates that blocked CBJs are well-represented in the WRF simulation along the  
486 windward side of the California coastal range at that time. However, during P2 (red and orange  
487 Xs) and afterward, combining the strong upstream winds and  $N_m$  produces a larger  $Fr$ , up to  
488 about 4 (e.g.,  $U = 20 \text{ m s}^{-1}$ ,  $N \sim 0.01 \text{ s}^{-1}$ ,  $h = 0.5 \text{ km}$ ). Thus the P2 TTA is not caused by terrain  
489 blocking. Comparable stabilities ( $N_m$ , ranging from 0.009 – 0.015) exist throughout P1-P3, but  
490 distinct flow patterns associated with different mechanisms occurred across the periods. The  
491 TTAs formed during P1 and P2 were likely produced by different processes, mainly related to a  
492 different source of the airmass.

493 Nearly all time during P1 had  $Fr < 1$ , regardless of the height of the terrain ( $h$ ), supporting an  
494 interpretation of a terrain blocked flow. However, most times during P2 and P3 had  $Fr > 1$ , with  
495 blocking only possible when  $h$  is large. Valenzuela and Kingsmill (2018) showed that in their  
496 study TTA terrain blocking was likely associated with high inland orography. Here, however, it  
497 appears that low-level blocking can also be generated by relatively low coastal orography ( $h \sim$

498 500 m elevation), although it is relatively weaker and more short lived than terrain blocking in  
499 the Valenzuela and Kingsmill study.

500 Following P1, but before the second TTA develops in P2, both coastal and mountain  
501 precipitation decreases significantly (Figs. 4b, 6) due to a reduction of moisture and temperature  
502 inland (not shown). This can be seen in Figs. 2(h, i) when there is a deep penetration of dry, cold  
503 air down to the mid-troposphere ( $\sim 500$  hPa), associated with the large-scale upper-level trough.  
504 In addition to changes in precipitation amount, Hughes et al. (2009) found that the ratio of  
505 precipitation at mountain (steepest slopes  $\sim 80$  m km<sup>-1</sup>) and coastal (gentlest slopes  $\sim 10$  m km<sup>-1</sup>)  
506 sites was close to 1:1 for low  $Fr$  but increased to nearly 4:1 for high  $Fr$ . This is consistent with  
507 our result of more coastal precipitation during P1 with low  $Fr$ , P2 with high  $Fr$ , and relatively  
508 more mountain precipitation during P3 with high  $Fr$  (Fig. 6d). Relationships suggested in Fig. 9  
509 could be strengthened in the future if additional offshore wind profile, temperature, and water  
510 vapor observations could be obtained to better estimate detailed fields of  $N_m$  and  $Fr$ .

511

### 512 *c. Mixing diagnostic*

513 The diagnostic  $Q$  is used to identify periods when stretching of airmasses increases  
514 interfacial area and thus facilitates mixing across boundaries. Figure 10a shows the time series  
515 of the  $Q$  calculated over BBY, CZD, and Mt. Santa Cruz (vertically averaged up to 700 hPa  
516 ( $\sim 3$ km)) during the study. The bottom panels are longitude-pressure cross-sections of  $Q$   
517 (averaged over 36.5-40°N) at the three periods indicated by vertical bars in panel (a). Also shown  
518 are water vapor mixing ratio overlaid by the zonal and vertical wind vector, interacting with the  
519 complex coastal mountains (see the upper panels of Figs. 10 (b, c, d)).

520 The time series of  $Q$  shows that regional differences in mixing between BBY and CZD are

521 small, with slightly less mixing expected in the Mt. Santa Cruz area during P2 and P3. All three  
522 locations show increasing mixing (more positive and high values of  $Q$ ) near the end of P2, with  
523 maxima in mid- (BBY and CDZ) to late- (Mt. Santa Cruz) P3 as the pre-cold frontal LLJ  
524 intensifies. During P1, enhanced water vapor ( $q$ ) is seen offshore and on the windward side of  
525 the mountain (124W-122.8°W) at 2300 UTC 10 March 2016. But  $Q$  is low both offshore and  
526 onshore, indicating mixing is weak during the low-level blocking period (Fig. 10b).

527 In contrast, during P2, easterly flow from inland, related to the gap flow from the mountain  
528 range, occurs at lower levels around 950 hPa ( $\sim 540$  m) by 1100 UTC. Strong ascending flow  
529 associated with the pre-cold frontal LLJ (wind speed  $> 20$  m s<sup>-1</sup>) occurs offshore during P2 and  
530 intensifies as the easterly, offshore-directed flow emerges in P3. The positive vertical motion  
531 was stronger offshore ( $> 124^\circ\text{W}$ ) than the windward side (124°W-122.8°W), while the negative  
532 vertical motion emerged over the lee side of the mountain ( $\sim 122^\circ\text{W}$ ) during P2. As the ascent  
533 and upslope IWV increases at the end of P2, precipitation was enhanced at the end of P2 (see Fig.  
534 4b). During P3, the mixing facilitates the lifting of the pre-cold frontal LLJs when the offshore-  
535 directed gap flow merges with the pre-cold frontal LLJs, which may enhance mountain  
536 precipitation and inland moisture transport (see Figs. 7d, 8i, Fig. S3 in Supplementary Materials).

537 The vertical motions during P2, P3 shown in the upper panels of Figs. 10(b, c, d) are  
538 consistent with the finding by Valenzuela and Kingsmill (2018), indicating that strong ascent  
539 occurs offshore over the TTA during TTA conditions while the ascent is slightly stronger over  
540 the coastal mountain during non-TTA periods. The model-simulated vertical motions in P1 in  
541 our study show that weak ascent occurs offshore, especially when averaging over the small area  
542 where the terrain-blocking flow is observed (the upper panel of Fig. 10b). The mixing was mild  
543 in P1, increasing in P2, and stronger over the coast and coastal mountain in P3 (the lower panels



544 in Figs. 10(b-d)). Overall, Fig. 10 quantitatively confirms that mixing between two air masses  
545 occurs during the end of P2 and P3, and it indeed affects the lifting of the pre-cold frontal LLJs  
546 toward the windward side of the coastal mountain, controlling the precipitation distribution by  
547 favoring mountain precipitation when the pre-cold frontal LLJs are lifted over the mountain,  
548 especially during P3.

549

## 550 **5. Summary and Conclusions**

551 We have characterized the evolving relationships between terrain trapped airflows (TTAs),  
552 synoptic-scale meteorological conditions, and precipitation in northern California during the  
553 Atmospheric River (AR) event of 10-11 March 2016 using aircraft measurements, surface  
554 observations, wind profiler data, and a 1-km resolution regional WRF simulation. We  
555 hypothesized that significant near coastal wind variations are related to different mechanisms for  
556 TTA formation, and that these wind variations have distinct impacts on precipitation locations  
557 and intensities during the evolution of an AR event. Two processes leading to TTA formation  
558 were identified: 1) low-level terrain blocking (i.e., coastal barrier jet; CBJ) and 2) offshore-  
559 directed gap flow augmenting more coast-parallel synoptic-scale flow.

560 The two mechanisms led to TTAs at different times during this event. The low-level blocking  
561 mechanism was identified when horizontal wind direction backed from synoptic-scale westerly  
562 flow well offshore to more southerly flow close to the coast in a regime with a Froude number  
563 ( $Fr$ )  $< 1$ . The gap flow mechanism was identified when the relationship between the offshore-  
564 directed near-surface wind and the pressure difference between entrance and exit of the Petaluma  
565 gap followed the gap flow force balance in a regime with  $Fr > 1$ . During both of these TTAs,

566 strong low pressure was centered offshore in association with a deep upper-level trough  
567 approaching the coast, with dry and relatively colder air inland.

568 The first type of TTA (a CBJ) occurred at the early stages of the AR event (period 1, P1) and  
569 it was associated with a maritime source of the air, relatively weak onshore flow, and a statically  
570 stable low-level environment. Shallow terrain blocking led to the TTA, although the magnitude  
571 of the coastal-parallel flow enhancement was weak, with surface wind speed less than  $5 \text{ m s}^{-1}$ .  
572 During this period, both surface measurements and model simulations showed relatively more  
573 coastal than mountain precipitation. Valenzuela and Kingsmill (2018) found that in their study  
574 terrain blocking was likely connected to higher inland terrain. Our results show that terrain  
575 blocking can also result from the effects of the lower coastal orography ( $h \sim 500 \text{ m}$  altitude).  
576 This result suggests that weak, transient CBJs may also be formed by shallow coastal mountain  
577 blocking in sufficiently weak onshore flows and high low-level static stability, whereas larger  
578 scale and more intense terrain blocking with stronger onshore flows as in Valenzuela and  
579 Kingsmill may be connected to higher orography of the Sierras.

580 The second type of TTA formed in a fundamentally different regime than during P1. In period  
581 2 (P2), winds strengthened with a component directed offshore. Our analysis showed that the  
582 formation of this TTA was due to offshore-directed gap-exit flow caused by the pressure and the  
583 temperature differences between the inland gap entrance and the coastal gap exit. The TTA  
584 during P2 exhibited surface wind speeds up to  $\sim 15 \text{ m s}^{-1}$ . Both TTAs extended offshore under  
585 100 km, less than the Rossby radius of deformation (Loescher et al. 2006; Luna-Niño and  
586 Cavazos 2017). The maximum speed of the TTA in P2 was roughly 2-3 times larger than that of  
587 the ambient synoptic flow. As P2 progressed, the confluence of the TTA with an approaching  
588 pre-cold frontal low-level jet (LLJ) led to the third AR period (period 3, P3). The P3 was

589 characterized by more intense mountain precipitation and stronger wind speeds ( $> 15 \text{ m s}^{-1}$ ) over  
590 the ocean and inland. Table 1 summarizes primary meteorological differences over the three  
591 periods.

592 Varying kinematic and thermodynamic characteristics between P1, P2, and P3 were closely  
593 associated with physical mechanisms for TTA formation, as well as interactions with the pre-  
594 cold frontal LLJ, which led to widely varying precipitation spatial distributions and intensities.  
595 The first TTA was associated with coastal terrain blocking and favored coastal rather than  
596 mountain precipitation, consistent with earlier findings. The  $Q$  diagnostic indicated that  
597 dynamical mixing likely elevated the pre-cold frontal LLJs, shifting high water vapor initially  
598 offshore and over the coastal regions onshore toward higher elevations inland, providing  
599 evidence for another mechanism influencing precipitation beyond what could be identified from  
600 previous single-point observations.

601 This study also showed that cold and dry air accompanied by a large-scale upper-level  
602 potential vorticity (PV) trough over northern California could facilitate the formation and  
603 development of TTAs, but more research is required to clarify to what extent such upper-level  
604 features affect the formation of low-level TTAs. Other variables or conditions influencing TTA  
605 development, characteristics, and impacts also merit further investigation, including the  
606 residence time of low-level water vapor flux, change in the atmospheric stability, and low-level  
607 shear-generated turbulence to alter orographic precipitation during the evolution of AR events.

608 Our study is unique in describing TTA formation from two distinct forcing mechanisms  
609 during different stages in the evolution of a single AR event. The results indicate that TTAs can  
610 substantially affect the timing, locations, and intensity of precipitation in California during such  
611 events. Similar effects appear likely to occur as well elsewhere along the U.S. West Coast.

612 Further work to better observe, understand, and model TTAs will help build the scientific basis  
613 for improving forecasts and early warnings of high-impact weather from AR events that so  
614 commonly affect the U.S. West Coast as well as many other coastal regions around the world  
615 with complex terrain.

616

617 **Acknowledgments**

618 The authors gratefully appreciate the support and partnership of H211 L.L.C, with particular  
619 thanks to the pilots, R. Simone and T. Grundherr, who flew expertly in bad weather to get AJAX  
620 data. We give special thanks to Warren J. Gore for his support on aircraft preparation and  
621 measurement. We are also grateful for comments and suggestions from Benjamin J. Moore and  
622 R. Bradley Pierce of NOAA. We appreciate the NOAA ESRL PSD wind profiler data and plots  
623 from <https://www.esrl.noaa.gov/psd/data/obs/datadisplay/>. Funding was provided by the NASA  
624 Postdoctoral Program, the Bay Area Environmental Research Institute, Science and Technology  
625 Corporation, and Scripps Institution of Oceanography, University of California San Diego. This  
626 research was also partly supported by the NASA Office of Education’s Minority University  
627 Research and Education Project (MUREP) Institutional Research Opportunity (MIRO) Contract  
628 #NNX15AQ02A. Funding for instrumentation and aircraft integration is gratefully  
629 acknowledged from Ames Research Center Director’s funds. The views, opinions, and findings  
630 contained in this report are those of the author(s) and should not be construed as an official  
631 National Oceanic and Atmospheric Administration or U.S. Government position, policy, or  
632 decision. Resources supporting this work were provided by the NASA High-End Computing  
633 (HEC) Program through the NASA Advanced Supercomputing (NAS) Division at NASA Ames  
634 Research Center and the NASA Center for Climate simulation (NCCS). We thank the editor  
635 and anonymous reviewers for their very thorough and valuable comments that have helped the  
636 authors to significantly improve the manuscript.

637

638 **References**

- 639 Bell, G. D., and L. F. Bosart, 1988: Appalachian cold-air damming. *Mon. Wea. Rev.*, **116**, 137–  
640 161.
- 641 Bosilovich, M.G., Lucchesi, R., Suarez, M., 2016: MERRA-2: File Specification. GMAO Office  
642 Note No. 9 (Version 1.1), 73 pp, available from.  
643 [http://gmao.gsfc.nasa.gov/pubs/office\\_notes](http://gmao.gsfc.nasa.gov/pubs/office_notes).
- 644 Browning, K. A., and C. W. Pardoe, 1973: Structure of low-level jet streams ahead of mid-  
645 latitude cold fronts. *Quart. J. Roy. Meteor. Soc.*, **99**, 619–638.
- 646 Chou, M. D., and M. J. Suarez, 1994: An efficient thermal infrared radiation parameterization for  
647 use in general circulation models. Technical Report, 85 p,  
648 <http://citeseerx.ist.psu.edu/viewdoc/summary?doi=10.1.1.26.4850>.
- 649 Chen, H., et al., 2010: High-accuracy continuous airborne measurements of greenhouse gases  
650 (CO<sub>2</sub> and CH<sub>4</sub>) using the cavity ring-down spectroscopy (CRDS) technique. *Atmos. Meas.*  
651 *Tech.*, **3**, 375-386.
- 652 Chen, W.-D., and R. B. Smith, 1987: Blocking and deflection of airflow by the Alps. *Mon. Wea.*  
653 *Rev.*, **115**, 2578–2597.
- 654 Colle, B. and C. F. Mass, 1995: The structure and evolution of cold surges east of the rocky  
655 mountains. *Mon. Wea. Rev.*, **123**, 2577–2610.
- 656 Colle, B., K. A. Loescher,, G. S. Young, N. S. Winstead, 2006: Climatology of Barrier Jets along  
657 the Alaskan Coast. Part II: Large-Scale and Sounding Composites, *Mon. Wea. Rev.*, **134**,  
658 454-477.
- 659 Dettinger, M., 2011a: Climate change, atmospheric rivers, and floods in California – a  
660 multimodel analysis of storm frequency and magnitude changes. *J. American Water*  
661 *Resources Association (JAWRA)*, **47(3)**:514–523, doi:19.1111/j.1752-1688.2011.00546.x.
- 662 Dettinger, M., F. M. Ralph, T. Das, P. J. Neiman, and D. R. Cayan, 2011b: Atmospheric rivers,  
663 floods, and the water resources of California. *Water*, **3**, 445–478, doi:10.3390/w3020445.
- 664 Doyle, J. D., 1997: The influence of mesoscale orography on a coastal jet and rainband. *Mon.*  
665 *Wea. Rev.*, **125**, 1465–1488.
- 666 Doyle, J. D., and T. T. Warner, 1993: A three-dimensional numerical investigation of a Carolina  
667 coastal low-level jet during GALE IOP 2. *Mon. Wea. Rev.*, **121**, 1030–1047.

668 Durrán, D. R., and J. B. Klemp, 1982: On the effects of moisture on the Brunt-Väilälä Frequency,  
669 *J. Atmos. Sci.*, **39**, 2152-2158.

670 Eiserloh, A. J, and S. Chiao, 2015: Modeling studies of landfalling atmospheric rivers and  
671 orographic precipitation over northern California, *Meteorology and Atmospheric Physics*,  
672 **127**, 1-16.

673 Ek, M. B., K. E. Mitchell, Y. Lin, E. Rogers, P. Grunmann, V. Koren, G. Gayno, and J. D.  
674 Tarpley, 2003: Implementation of Noah land surface model advances in the National  
675 Centers for Environmental Prediction operational mesoscale Eta model. *J. Geophys. Res.*,  
676 **103**, D22, 8851, doi: 10.1029/2002JD003296.

677 Fairlie, T.D., Avery, M. A., Pierce, R.B., Al-Saadi, J., Dibb, J., Sachse, G., 2007: Impact of  
678 multiscale dynamical processes and mixing on the chemical composition of the upper  
679 troposphere and lower stratosphere during the Intercontinental Chemical Transport  
680 Experiment–North America, *J. Geophys. Res. Atmos.*, **112**, D16S90,  
681 doi:10.1029/2006JD007923.

682 Filges, A., C. Gerbig, H. Chen, H. Franke, C. Klaus, and A. Jordan, 2015: The IAGOS-core  
683 greenhouse gas package: a measurement system for continuous airborne observations of  
684 CO<sub>2</sub>, CH<sub>4</sub>, H<sub>2</sub>O and CO, *Tellus B*, **67**, 27989, <https://doi.org/10.3402/tellusb.v67.27989>.

685 Gaines, S. E., S. W. Bowen, R. S. Hipskind, T.P. Bui, and K. R. Chan, 1992: Comparisons of the  
686 NASA ER-2 meteorological measurement system with radar tracking and radiosonde data, *J.*  
687 *Atmos. Ocean. Tech.*, **9**, 210-225.

688 Galewsky, J., and A. Sobel, 2005: Moist Dynamics and Orographic Precipitation in Northern and  
689 Central California during the New Year’s Flood of 1997, *Mon., Wea. Rev.*, **133**, 1594-1612.

690 Gill, A.E., 1982: Atmosphere–Ocean Dynamics. Academic Press: Orlando, FL.

691 Guan, B., N. P. Molotch, D. E. Waliser, E. J. Fetzer, and P. J. Neiman, 2013: The 2010/2011  
692 snow season in California's Sierra Nevada: Role of atmospheric rivers and modes of large-  
693 scale variability. *Water Resour. Res.*, **49**, 6731-6743, doi:10.1002/wrcr.20537.

694 Hamill, P., L. T. Iraci, E. L. Yates, W. Gore, T. P. Bui, T. Tanaka, and M. Loewenstein, 2016: A  
695 new instrumented airborne platform for atmospheric research, *Bull. Amer. Meteo. Soc.*, 397-  
696 404.

697 Haynes, P.H., 1990. High-resolution three-dimensional modeling of stratospheric flows: quasi-  
698 two-dimensional turbulence dominated by a single vortex, *Topological Fluid Mechanics*.  
699 Cambridge Univ. Press, New York, pp. 345-354.

700 Hong, S. Y., Y. Noh, J. Dudhia, 2006: A new vertical diffusion package with an explicit treatment  
701 of entrainment processes. *Mon. Wea. Rev.*, **134**, 2318–2341. doi:10.1175/MWR3199.1

702 Houze, R. A., Jr., and S. Medina, 2005: Turbulence as a mechanism for orographic precipitation  
703 enhancement. *J. Atmos. Sci.*, **62**, 3599–3623, doi:10.1175/JAS3555.1.

704 Hughes, M., A. Hall, and R. G. Fovell, 2009: Blocking in Areas of Complex Topography, and its  
705 influence on rainfall distribution, *J. Atmos. Sci.*, **66**, 508-518, DOI: 10.1175/2008JAS2689.1

706 Jankov, I., P. J. Schultz, C. J. Anderson, and S. E. Koch, 2007: The impact of different physical  
707 parameterizations and their interactions on cold season QPF in the American River Basin. *J.*  
708 *Hydrometeo.*, **8**, 1141–1151.

709 Kim, J., H.-S. Kang, 2007: The impact of the Sierra Nevada on low-level winds and water vapor  
710 transport, *J. Hydrometeo.*, **8**, 790-804.

711 Loescher, K. A., G. S. Young, B. A. Colle, and N. S. Winstead, 2006: Climatology of barrier jets  
712 along the Alaskan coast. Part I: Spatial and temporal distributions. *Mon. Wea. Rev.*, **134(2)**,  
713 437-453.

714 Luna-Nino, R., T. Cavazos, 2017: Formation of a coastal barrier jet in the Gulf of Mexico due to  
715 the interaction of cold fronts with the Sierra Madre Oriental mountain range, *Q., J. R.*  
716 *Meteorol., Soc.*, DOI:10.1002/qj.3188.

717 Martin, A., Ralph, F.M., Demirdjian, R., DeHaan, L., Weihs, R., Helly, J., Reynolds, D. and  
718 Iacobellis, S., 2018. Evaluation of Atmospheric River Predictions by the WRF Model Using  
719 Aircraft and Regional Mesonet Observations of Orographic Precipitation and Its Forcing. *J.*  
720 *Hydrometeo.*, **19(7)**, pp.1097-1113.

721 Mass, C. F., S. Businger, M.D. Albright, and Z. A. Tucker, 1995: A windstorm in the lee of a gap  
722 in a coastal mountain barrier. *Mon. Wea. Rev.*, **123(2)**, 315-331.

723 Mlawer, E. J., S. J. Taubman, P. D. Brown, M J. Iacono, and S. A. Clough, 1997: Radiative  
724 transfer for inhomogeneous atmospheres: RRTM, a validated correlated-k model for the  
725 longwave, *J. Geophys. Res.*, **102**, 16663-16682.



726 Neiman, P. J., F. M. Ralph, A. B. White, D. E. Kingsmill, and P. O. G. Persson, 2002: The  
727 statistical relationship between upslope flow and rainfall in California's coastal mountains:  
728 Observations during CALJET. *Mon. Wea. Rev.*, **130**, 1468–1492.

729 \_\_\_\_\_, F. M. Ralph, A. B. White, D. Parrish, J. S. Holloway, and D. L. Bartels, 2006: A  
730 multiwinter analysis of channeled flow through a prominent gap along the northern  
731 California coast during CALJET and PACJET. *Mon. Wea. Rev.*, **134**, 1815–1841,  
732 doi:10.1175/MWR3148.1

733 \_\_\_\_\_, F. M. Ralph, G. A. Wick, J. D. Lundquist, and M. D. Dettinger, 2008: Meteorological  
734 characteristics and overland precipitation impacts of atmospheric rivers affecting the west  
735 coast of North America based on eight years of SSM/I satellite observations. *J. Hydrometeo.*,  
736 **9**, 22–47.

737 \_\_\_\_\_, E.M. Sukovich, F. M. Ralph, and M. Hughes, 2010: A seven year wind profiler-based  
738 climatology of the windward barrier jet along California's northern Sierra Nevada. *Mon.*  
739 *Wea. Rev.*, **138**, 1206–1233, doi:10.1175/2009MWR3170.1.

740 \_\_\_\_\_, M. Hughes, B. J. Moore, F. M. Ralph, E. M. Sukovich, 2013: Sierra barrier jets,  
741 atmospheric rivers, and precipitation characteristics in northern California: a composite  
742 perspective based on a network of wind profilers. *Mon. Wea. Rev.*, **141**, 4211–4233, doi:  
743 10.1175/MWR-D-13-00112.1

744 \_\_\_\_\_, F. M. Ralph, B J. Moore, R. J. Zamora, 2014: The regional influence of an intense  
745 sierra barrier jet and landfalling atmospheric river on orographic precipitation in northern  
746 California: a case study. *J. Hydrometeo.*, **140**, 358–378, DOI: 10.1175/JHM-D-13-0183.1.

747 Nelson, B. R., O. P. Prat, D.-J. Seo, E. Habib, 2016: Assessment and Implications of NCEP Stage  
748 IV Quantitative Precipitation Estimates for Product Intercomparisons, *Weather and*  
749 *Forecasting*, **31**, 371 – 394.

750 Olson, J. B., B. A. Colle, N. A. Bond, N. Winstead, 2007: A comparison of two coastal barrier jet  
751 events along the southeast Alaskan coast during the SARJET field experiment. *Mon. Wea.*  
752 *Rev.*, **135**, 2973–2994, DOI: 10.1175/MWR3448.1.

753 Parish, T. R., 1982: Barrier winds along the Sierra Nevada mountains, *J. Appl. Meteo.*, **21**, 925-  
754 930.

755 Pierrehumbert, R. T., and B. Wyman, 1985: Upstream effects of mesoscale mountains. *J. Atmos.*  
756 *Sci.*, **42**, 977-1003.

757 Ralph, F. M., P. J. Neiman, and G. A. Wick, 2004: Satellite and CALJET aircraft observations of  
758 atmospheric rivers over the eastern North Pacific Ocean during the El Nino winter of  
759 1997/98. *Mon. Wea. Rev.*, **132**, 1721–1745.

760 \_\_\_\_\_, \_\_\_\_\_, and R. Rotunno, 2005a: Dropsonde observations in low-level jets over the  
761 northeastern Pacific Ocean from CALJET-1998 and PACJET-2001: mean vertical-profile  
762 and atmospheric-river characteristics. *Mon. Wea. Rev.*, **133**, 889–910.

763 \_\_\_\_\_, \_\_\_\_\_, and Coauthors, 2005b: Improving short-term (0–48 h) cool season  
764 quantitative precipitation forecasting: Recommendations from a USWRP workshop. *Bull.*  
765 *Amer. Meteor. Soc.*, **86**, 1619–1632.

766 \_\_\_\_\_, \_\_\_\_\_, G. A. Wick, S. I. Gutman, M. D. Dettinger, D. R. Cayan, and A. B., White,  
767 2006: Flooding on California’s Russian River: The role of atmospheric rivers. *Geophys. Res.*  
768 *Lett.*, **33**, L13801, doi:10.1029/2006GL026689.

769 Ryoo, J.-M., D. E. Waliser, D. W. Waugh, S. Wong, E. J. Fetzer, and I. Fung, 2015:  
770 Classification of atmospheric river events on the U.S. West Coast using a trajectory model,  
771 *J. Geophys. Res. Atmos.*, **120**, doi:10.1002/2014JD022023.

772 Scott, S.G., T.P. Bui, K. R. Chan, and S. W. Bowen, 1990: The meteorological measurement  
773 system on the NASA ER-2 aircraft, *J. Atmos. Ocean. Tech.*, **7**, 525-540.

774 Skamarock, W. C., et al., 2008: A description of the Advanced Research WRF version 3. NCAR  
775 Tech Note NCAR/TN-475 + STR, 113 pp, doi:10.5065/D68S4MVH.  
776 [http://www.mmm.ucar.edu/wrf/users/docs/arw\\_v3.pdf](http://www.mmm.ucar.edu/wrf/users/docs/arw_v3.pdf)

777 Smalley, M., T. L’Ecuyer, M. Lebsock, J. Haynes, 2013: A comparison of precipitation  
778 occurrence from the NCEP Stage IV QPE product and the CloudSat cloud profiling radar. *J.*  
779 *Hydrometeo.*, **15**, 444-458, doi:10.1175/JHM-D-13-048.1

780 Smith, A. L., S. E. Yuter, P. J. Neiman, D. E. Kingsmill, 2010: Water vapor fluxes and orographic  
781 precipitation over northern California associated with a landfalling atmospheric river. *Mon.*  
782 *Wea. Rev.*, **138**, 74–100, DOI: 10.1175/2009MWR2939.1.

783 Steenburgh, W. J., D. M. Schultz, and B. A. Colle, 1998: The structure and evolution of gap  
784 outflow over the gulf of tehuatepec, Mexico, *Mon. Wea. Rev.*, **126**, 2673-2691.

785 Strangeways, I. C., 1996: Back to basics: the ‘met. enclosure’: Part 2(b)—Raingauges, their errors.  
786 *Weather*, **51**, 298–303.

787 Thompson, G, R.M. Rasmussen, K. Manning, 2004: Explicit forecasts of winter precipitation  
788 using an improved bulk microphysics scheme. part I: description and sensitivity analysis.  
789 *Mon. Wea. Rev.*, **132**, 519–542.

790 Valenzuela, R., and D. E. Kingsmill, 2015: Orographic precipitation forcing along the coast of  
791 Northern California during a landfalling winter storm. *Mon. Wea. Rev.*, **143(9)**. 3570-3590.  
792 Doi:10.1175/MWR-D-14-00365.1.

793 \_\_\_\_\_, and \_\_\_\_\_, 2017: Terrain-trapped airflows and orographic rainfall along the coast of  
794 northern California. Part I: Kinematic characterization using a wind profiling radar. *Mon.*  
795 *Wea. Rev.*, **145(8)**, 2993-3008, doi:10.1175/MWR-D-16-0484.1.

796 \_\_\_\_\_, and \_\_\_\_\_, 2018: Terrain-trapped Airflows and Orographic Rainfall along the Cost  
797 of Northern California. Part II: Horizontal and vertical structures observed by a scanning  
798 Doppler radar. *Mon. Wea. Rev.*, **146**, 2381-2402, DOI: 10.1175/MWR-D-17-0227.1.

799 White, A. B., M. L. Anderson, M. D. Dettinger, F. M. Ralph, A. Hinojosa, D. R. Cayan, R. K.  
800 Hartman, D. W. Reynolds, L. E. Johnson, T. L. Schneider, R. Cifelli, Z. Toth, S. I. Gutman,  
801 C. W. King, F. Gehrke, P.E. Johnston, C. Walls, D. Mann, D. J. Gottas, and T. Coleman,  
802 2013: A Twenty-First-Century California Observing Network for Monitoring Extreme  
803 Weather Events, *J. Atmos. Ocean. Techno.* **30**, 1585-1603, DOI: 10.1175/JTECH-D-12-  
804 00217.1.

805 Wick, G. A., P. J. Neiman, and F. M. Ralph, 2013a: Description and validation of an automated  
806 objective technique for identification and characterization of the integrated water vapor  
807 signature of atmospheric rivers, *IEEE TRANSACTIONS ON GEOSCIENCE AND*  
808 *REMOTE SENSING*, VOL. 51, NO. 4, 2166-2176.

809 Wick, G. A., P. J. Neiman, F. M. Ralph, and T. M. Hamill, 2013b: Evaluation of forecasts of the  
810 water vapor signature of atmospheric rivers in operational numerical weather prediction  
811 models., *Wea. Forecast*, **28**, 1337-1352.

812 Yu, C.-K., and B. F. Smull, 2000: Airborne observations of a landfalling cold front upstream of  
813 steep coastal orography. *Mon. Wea. Rev.*, **128**, 674–692.

814 Zhu, Y., and R. E. Newell, 1994: Atmospheric rivers and bombs. *Geophys. Res. Lett.*, **21**, 1999–  
815 2002.

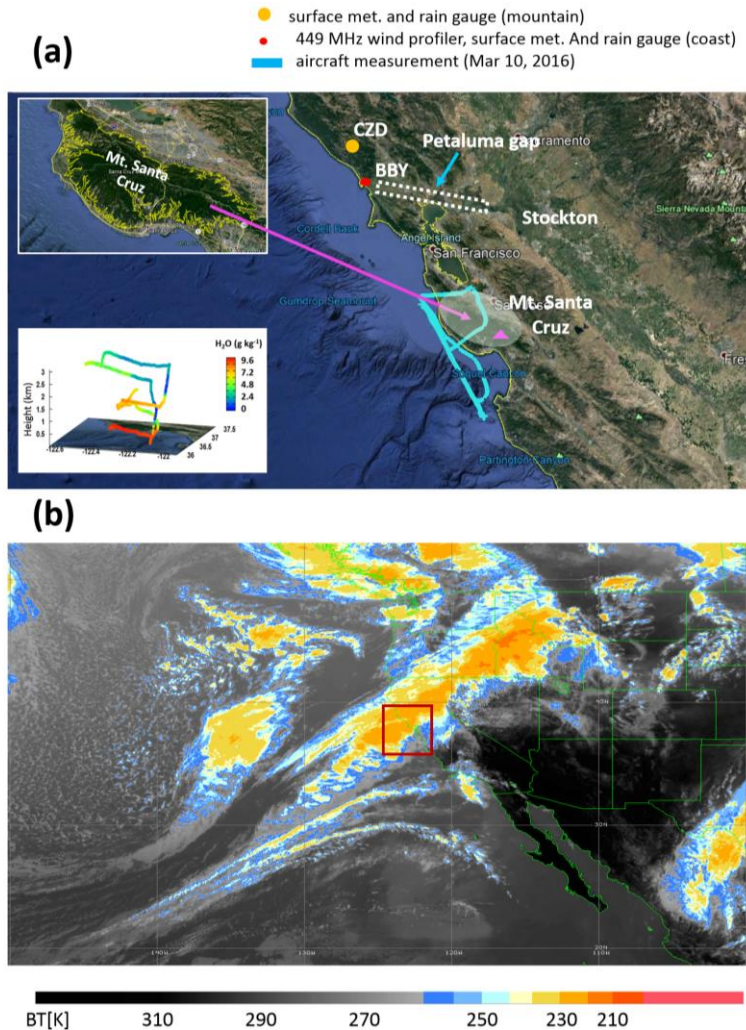
816 \_\_\_\_\_, and \_\_\_\_\_, 1998: A proposed algorithm for moisture fluxes from atmospheric rivers.  
817 *Mon. Wea. Rev.*, **126**, 725–735.

818 **Table 1.** Characteristics of TTAs and precipitation over different periods (P1, P2, and P3) during  
 819 10-11 March 2016 AR events over BBY and Mt. Santa Cruz. The low-level wind defines wind  
 820 below 800 m.  
 821

Period	Period 1 (P1)	Period 2 (P2)	Period 3 (P3)
<b>Start</b>	2100 UTC 10 March 2016	0500 UTC 11 March 2016	1000 UTC 11 March 2016
<b>End</b>	2300 UTC 10 March 2016	0900 UTC 11 March 2016	1800 UTC 11 March 2016
<b>Low-level (&lt; ~ 800 m) wind direction</b>	Onshore-directing deflected wind pattern toward the coast, southeasterly	Offshore-directing wind, southeasterly	Southeasterly and southwesterly
<b>Low-level (&lt; ~ 800 m) wind speed</b>	< 5 m s <sup>-1</sup>	< 15 m s <sup>-1</sup>	> 15 m s <sup>-1</sup> ,
<b>Precipitation ratio (mountain/ coast (i.e. CZD/BBY))</b>	< 1.5 on average	< 1.5 on average	> 2.5 on average
<b>Low-level blocking (Coastal barrier jet formed)</b>	Yes	No	No
<b>LLJs</b>	Merge with pre-cold-frontal LLJs	Gap flows	No
<b>CBJs</b>	Yes (CBJs)	Yes (Gap flows)	Yes (Gap flows merge with pre-cold-frontal LLJs)
<b>Vertical motion</b>	Mild ascent offshore	Moderate ascent offshore	Strong ascent over the coastal mountain
<b>Observational data source</b>	AJAX aircraft data near Mt. Santa Cruz and wind profiler data over BBY, tipping bucket rain measurement	Wind profiler data over BBY, tipping bucket rain measurement	Wind profiler data over BBY, tipping bucket rain measurement
<b>Notes</b>	Low-level blocking (CBJ) due to the coastal terrain	Temperature difference between the Potluma gap entrance and exit	Gap flows merge with pre-cold-frontal LLJs

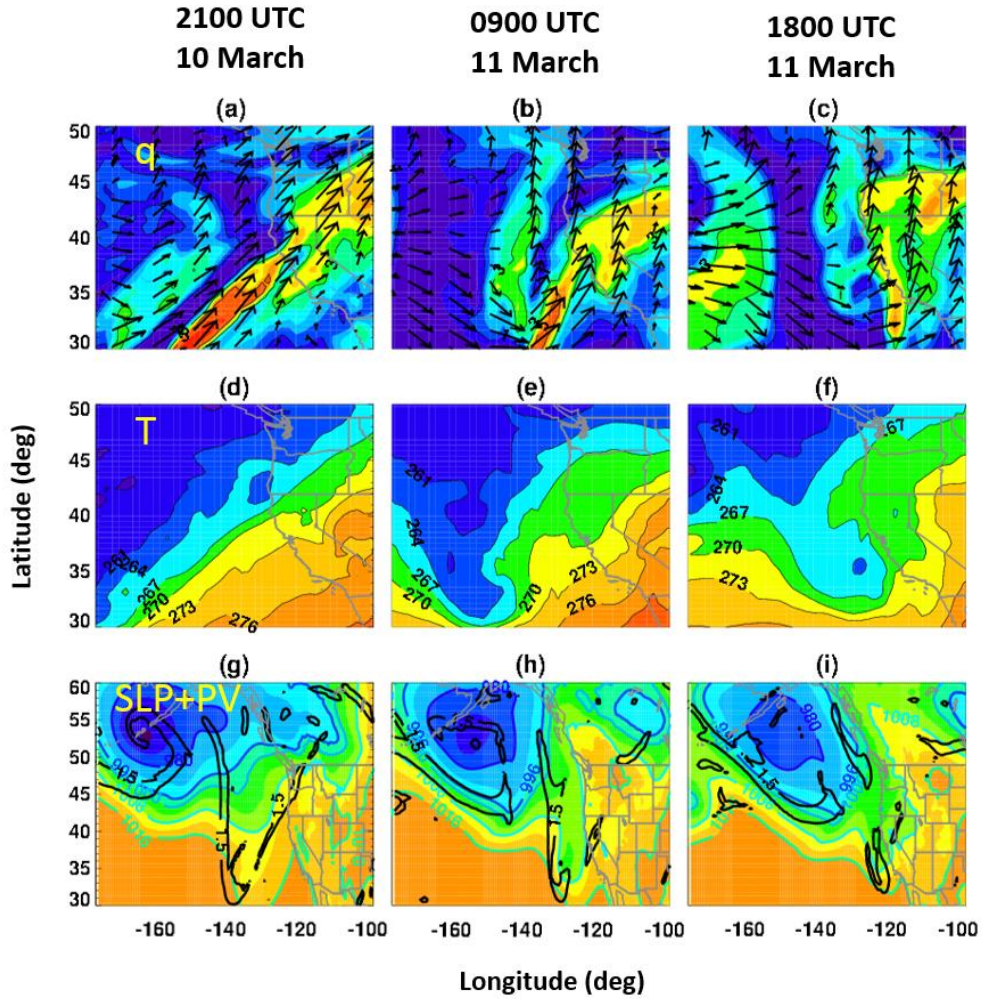
822

823



824

825 **Fig. 1.** (a) Map of the study region overlaid with observing systems. The legend identifies the  
 826 coastal (BBY) and mountain (CZD) measurement sites. Inset shows 3-D view of water vapor  
 827 mixing ratio [g kg<sup>-1</sup>] measured by the Alpha Jet Atmospheric eXperiment (AJAX) flight (upper)  
 828 from 2250 UTC 10 March 2016 to 0005 UTC 11 March 2016. (b) Satellite image of 10.7 μm  
 829 Brightness Temperature (in color) obtained from NASA Langley Cloud and Radiation Research  
 830 (from Geostationary Operational Environmental Satellite (GOES-15) Imagery and Cloud  
 831 Products) on 2230 UTC 10 March 2016. The red box indicates the area expanded in panel a).  
 832 The green area with the yellow line represents the Santa Cruz mountains (Mt. Santa Cruz) area.  
 833 The magenta triangle represents the peak of Mt. Santa Cruz.

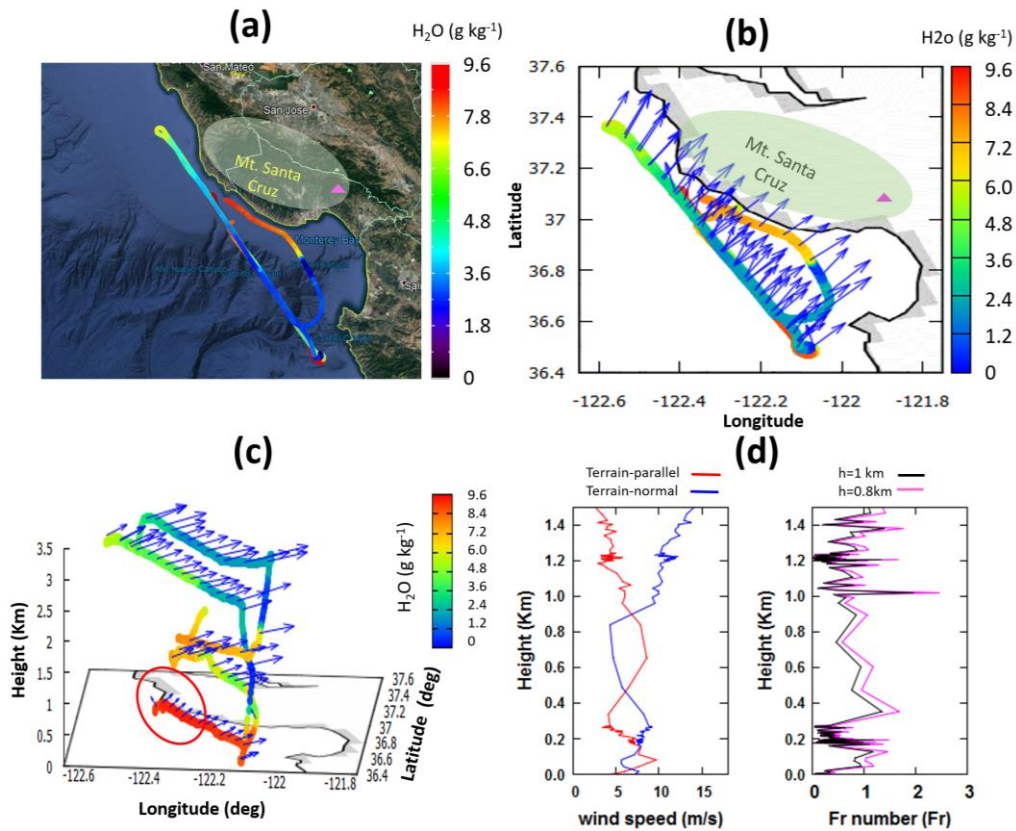


834

835 **Fig. 2.** Longitude-latitude cross-section of (a, b, c) water vapor mixing ratio [ $\text{g kg}^{-1}$ ] overlaid by  
 836 horizontal wind vector [ $\text{m s}^{-1}$ ] at 700 hPa; (d, e, f) temperature [K] at 700 hPa; and (g, h, i) sea  
 837 level pressure [hPa, in color] overlaid by potential vorticity (PV) at 500 hPa where  $\text{PVU} = 1.5$  ( $1$   
 838  $\text{PVU} = 10^{-6} \text{ m}^{-2} \text{ s}^{-1} \text{ K kg}^{-1}$ ) at (left) 2100 UTC 10 March 2016, (middle) 0900 UTC 11 March  
 839 2016, and (right) 1800 UTC 11 March 2016 obtained from the MERRA-2 reanalysis data.

840

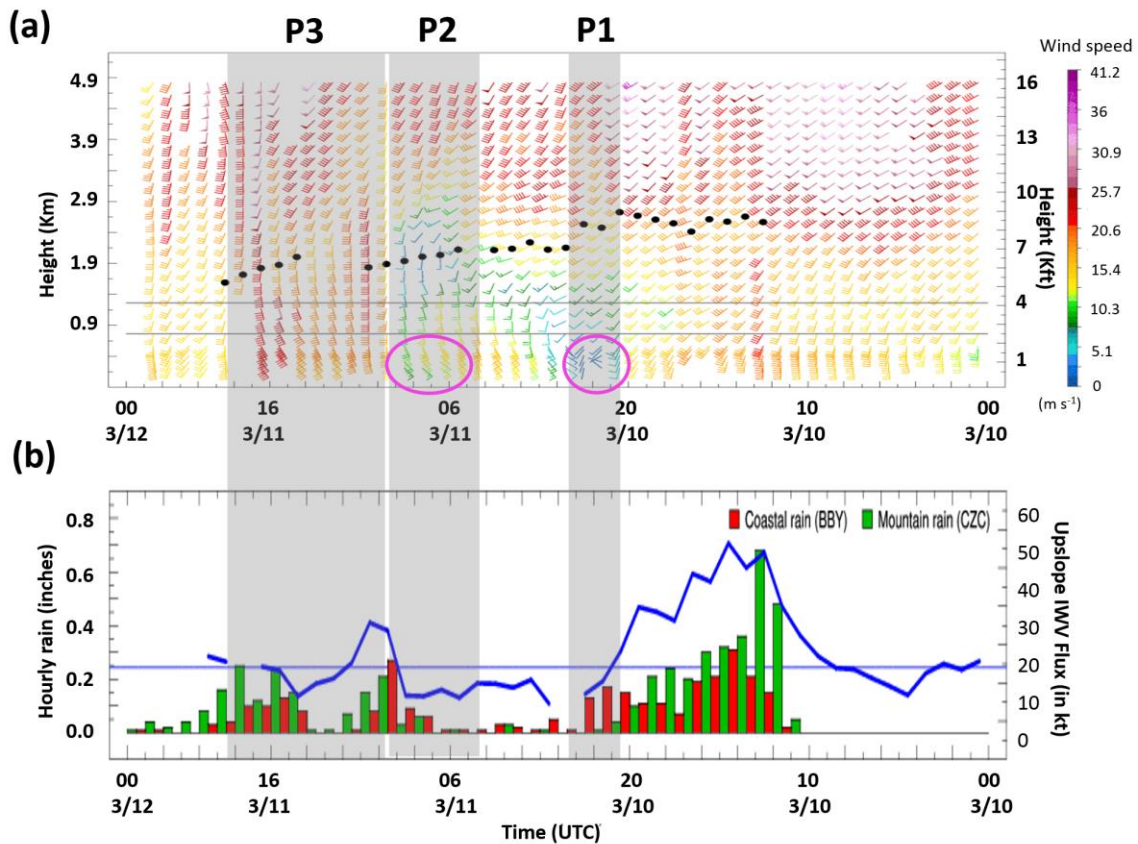




841

842 **Fig. 3** Maps of (a) measured water vapor and (b) wind along the Alpha Jet Atmospheric  
 843 eXperiment (AJAX) flight track. (c) Water vapor mixing ratio [ $g\ kg^{-1}$ ] overlaid with horizontal  
 844 wind vectors ( $[m\ s^{-1}]$ , blue) measured by AJAX flight. The red circle indicates the deflected flow  
 845 toward the coast along the transect from the southeast (SE) to the northwest (NW). (d) the  
 846 vertical profiles of terrain-parallel ( $[m\ s^{-1}]$ , red) and terrain-normal wind ( $[m\ s^{-1}]$ , blue), and  
 847 computed  $Fr$  (magenta, black) using AJAX data from 2250 UTC 10 March 2016 to 0005 UTC  
 848 11 March 2016. The magenta and black lines represent the  $Fr$  computed using different  
 849 mountain heights ( $h$ , 800 m and 1 km, respectively). The shaded circle (green) represents the  
 850 Santa Cruz mountains (Mt. Santa Cruz) area. The magenta triangle represents the peak of Mt.  
 851 Santa Cruz.

852

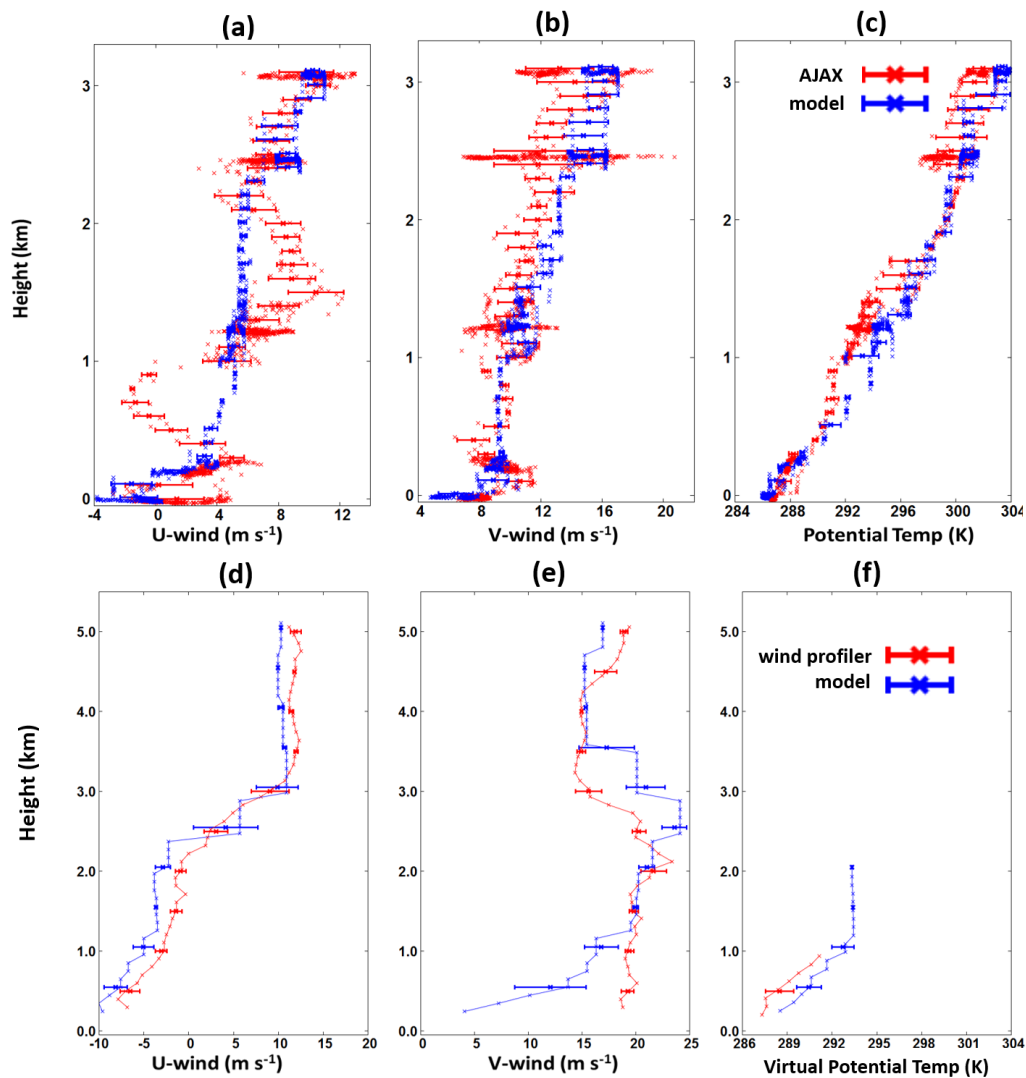


853

854

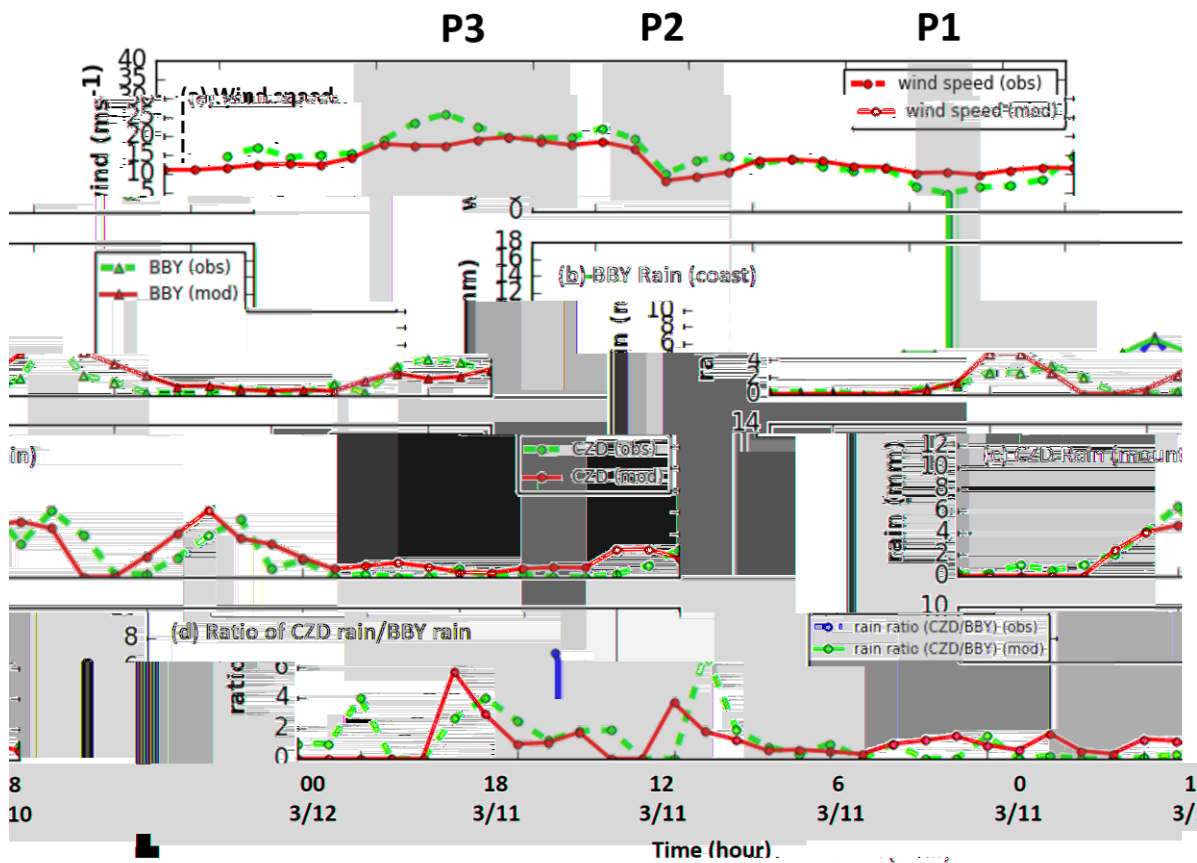
855 **Fig. 4.** Time series of (a) wind speed as a function of altitude at Bodega Bay (BBY, knots) and  
 856 (b) observed hourly precipitation (inches) over the BBY (coast, red) and the Cazadero (CZD,  
 857 mountain, green) sites, with the upslope integrated water vapor flux (blue, in knots) observed by  
 858 the wind profiler at BBY from 0000 UTC 10 March to 0000 UTC 12 March 2016. Gray-shaded  
 859 boxes in panels (a, b) identify the time periods for further discussion: P1 between 2100 – 2300  
 860 UTC 10 March, P2 during 0500 – 0900 UTC 11 March, and P3 during 1000 – 1800 UTC 11  
 861 March. The black dots in (a) represent the observed hourly profiler-derived snow level. The  
 862 figure is initially obtained from <https://www.esrl.noaa.gov/psd/data/obs/datadisply/>. Note that  
 863 the time axis is from right to left to represent the eastward advection of the AR storm. The  
 864 magenta circle during P1 and P2 refers to the occurrence of the first and the second TTA,  
 865 respectively.





866  
 867 **Fig. 5.** Vertical profiles of zonal wind ( $[m s^{-1}]$ , U-wind), meridional wind ( $[m s^{-1}]$ , V-wind), and  
 868 virtual potential temperature [K] (a, b, c) measured by AJAX flight (red) and modeled by WRF  
 869 model (blue) interpolated along the AJAX flight track from 2250 UTC 10 March 2016 to 0005  
 870 UTC 11 March 2016. (d, e, f) Measured by BBY wind profiler (red) and modeled by WRF  
 871 model (blue) along the wind profiler at 1100 UTC 11 March 2016. One standard deviation from  
 872 the mean value at each altitude is presented with the horizontal bar.

873



874

875 **Fig. 6.** Time series of (red) observed and (blue) modeled (a) wind speed at BBY (b) precipitation  
 876 over BBY (coastal region), (c) precipitation over CZD (mountain region), and (d) rain ratio  
 877 (CZD/BBY) from 1800 UTC 10 March to 0000 UTC 12 March 2016. Observed wind data is  
 878 only available over BBY from the wind profiler.

879

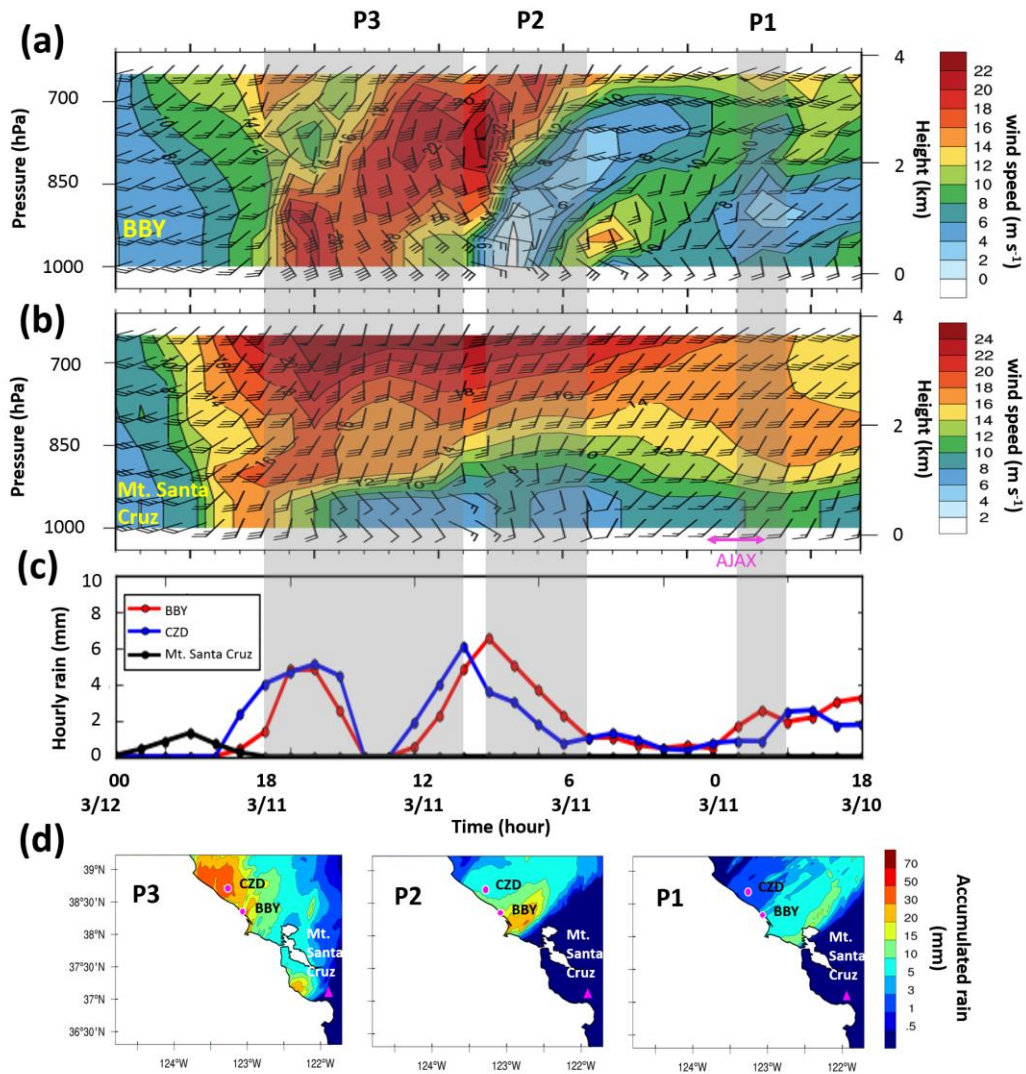
880

881

882

883

884

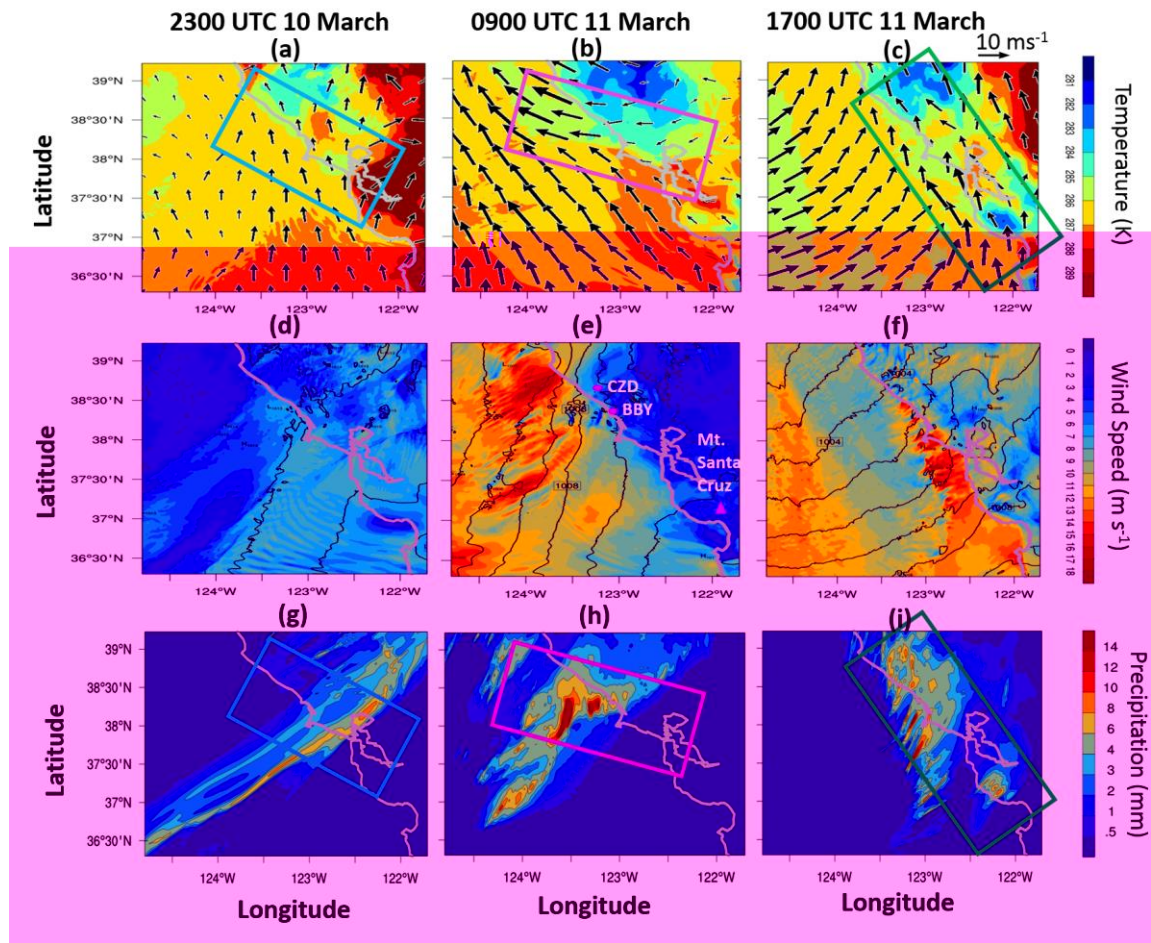


885

886 **Fig. 7.** Time-height cross-section of modeled meridional wind speed [ $\text{m s}^{-1}$ ] overlaid by the total  
 887 horizontal wind at (a) BBY and (b) Mt. Santa Cruz from WRF model simulation. Panels (c, d)  
 888 show modeled precipitation [mm] (c) at coastal (BBY) and mountain (CZD and Mt. Santa Cruz)  
 889 sites, and (d) averaged over the period P1, P2, and P3. The time axis in (a-c) is from right to left  
 890 to represent the eastward advection of the AR storm.

891

892

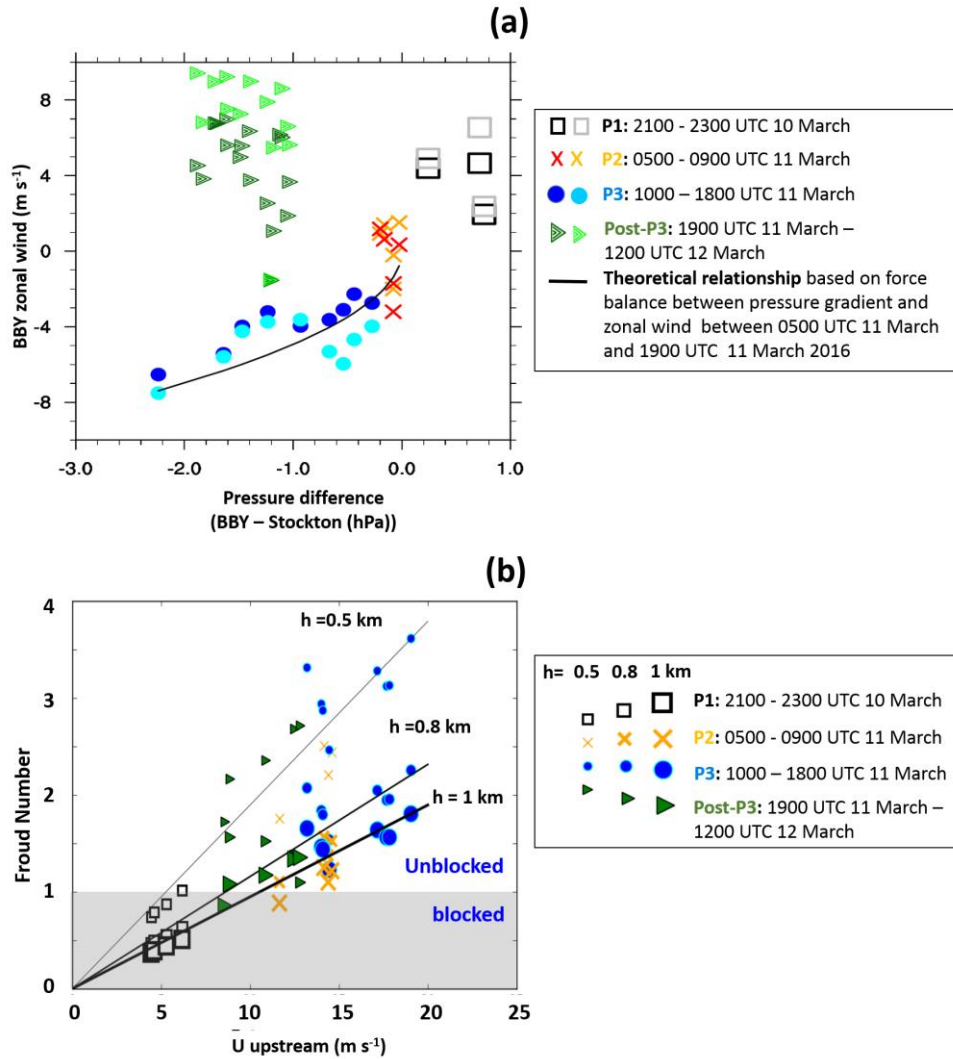


893

894 **Fig. 8.** WRF model-simulated (a, b, c) surface air temperature ([K], shaded) overlaid by 10-  
 895 meter wind vector (arrows), (d, e, f) 10-meter wind speed ([ $\text{m s}^{-1}$ ], shaded) overlaid by sea level  
 896 pressure (hPa, black line) and (g, h, i) model precipitation [mm] at (a, d, g) 2300 UTC 10 March,  
 897 (b, e, h) 0900 UTC 11 March, and (c, f, i) 1700 UTC 11 March 2016. Each box represents the (a)  
 898 onshore directing deflected flows, (b) offshore directing gap flows, and (c) pre-cold frontal LLJs  
 899 merging with offshore flows, respectively.

900

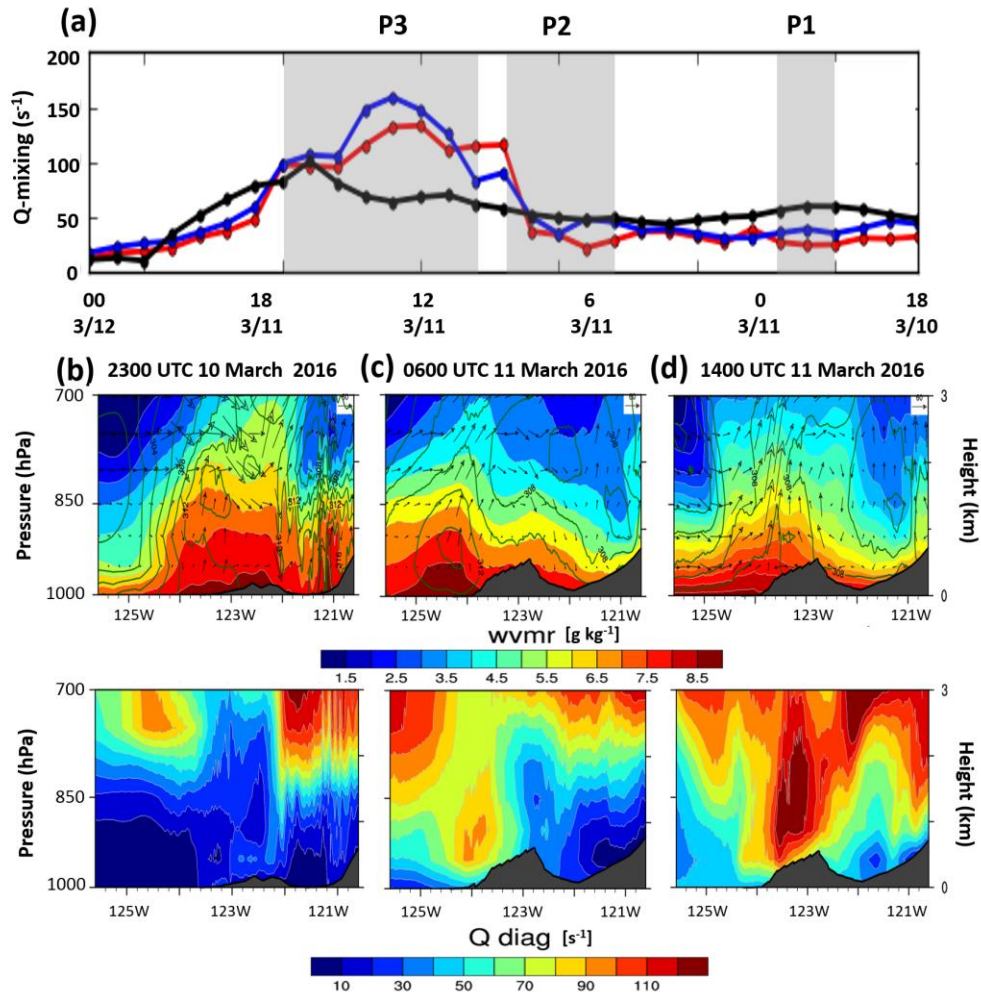
901



902

903 **Fig. 9. (a)** A scatter plot of the WRF model simulated hourly surface pressure difference  
 904 between BBY and Stockton, CA vs hourly surface zonal winds (black, red, blue, dark green) and  
 905 approximately below 500m layer averaged zonal wind (gray, orange, cyan, green) at BBY. The  
 906 black line in (a) stands for the theoretical relationship between pressure gradient, surface friction,  
 907 and gap flows provided by Mass et al. (1995) and Valenzuela and Kingsmill (2015). **(b)**  $Fr$   
 908 analysis using modeled upstream  $U$  [ $m s^{-1}$ ] and  $N_m$  [ $s^{-1}$ ] for different mountain height ( $h = 0.5,$   
 909  $0.8,$  and  $1$  km). Each regression was computed for  $U$  and  $Fr$  using different  $h$ . The different color  
 910 corresponds to a different period for P1 (black), P2 (orange), P3 (blue), and post-P3 (green). The  
 911 different size corresponds to different mountain height from 0.5 to 1 km (smallest to largest).  
 912 The gray box area is indicated as blocked when  $Fr$  is less than 1.





913

914 **Fig. 10.** (a) Time series of Q diagnostic [ $s^{-1}$ ] averaged over BBY (red), CZD (blue), Mt. Santa  
 915 Cruz (black) from 1800 UTC 10 March to 0000 UTC 12 March. (b-d) Longitude-pressure cross-  
 916 section of simulated (top panels) water vapor mixing ratio [ $g\ kg^{-1}$ ] and zonal (u) and vertical  
 917 wind (w) vector ([ $m\ s^{-1}$ ], w is multiplied by scale factor (100)), and (bottom panels) Q  
 918 diagnostic [ $s^{-1}$ ] averaged over 38-38.5°N at 2300 UTC 10 March, averaged over 36.5-40°N at  
 919 0600 UTC 11 March and 1400 UTC 11 March 2016, respectively.

920